Generic Modal Design Variables for Efficient Aerodynamic Optimisation

Laurence Kedward [†] ; C. Allen [‡] ; Daniel Poole [§] ; T. Rendall [¶]
Department of Aerospace Engineering, University of Bristol, Bristol, UK

Orthogonal modes are an effective method for aerodynamic shape optimisation due to their excellent design space compactness however all existing methods are generated from a database of representative geometry. Moreover, application to high-fidelity design spaces is not possible due to high-frequency shape components being insufficiently bounded leading to non-smooth and oscillatory geometries. In this work, a new generic methodology for generating orthogonal shape modes is presented based on a purely geometric derivation, eliminating the need for geometric training data. The new method is a further development of the gradient-limiting method developed previously for constraining the design space in a geometrically meaningful way to reduce the effective degrees of freedom and improve optimization convergence rate and final result. Here, the gradient-limiting methodology is reformulated by transforming the constraints directly onto design variables to produce orthogonal shape modes with equivalent constraints for ensuring smooth and valid iterates. The new generic methodology requires no training data, can be applied to arbitrary topologies using different boundary conditions and naturally includes translational modes as part of the orthogonal basis. When applied to two standard aerodynamic test cases, the new method has superior performance compared to library-derived modes. Importantly, the optimisation convergence rate is independent of the number of design variables and the optimised objective at high design fidelities is greatly improved by avoiding local minima corresponding to spurious geometries. A non-standard test case is demonstrated, for which traditional library modes are not useable due to non-trivial topology, and it is shown to benefit from the high-fidelity design space and translational mode made possible with the novel methodology.

Aspects of this work have been presented at AIAA SCITECH and AVIATION forums in papers 2020-0543 and 2020-2707.
[†]PhD Student, AIAA Student Member, laurence.kedward@bristol.ac.uk, Bristol, BS8 1TR, UK
[‡]Professor of Computational Aerodynamics, AIAA Senior Member, c.b.allen@bristol.ac.uk, Bristol, BS8 1TR, UK
[§]Senior Lecturer, AIAA Member, thomas.rendall@bristol.ac.uk, Bristol, BS8 1TR, UK
[¶]Associate Professor, AIAA Member, thomas.rendall@bristol.ac.uk, Bristol, BS8 1TR, UK

Nomenclature

C_D	=	Drag coefficient			
C_L	=	Lift coefficient			
C_M	=	Pitching moment coefficient	$\boldsymbol{\alpha}$	=	Design variable vector
$\bar{h}$	=	Mean surface mesh spacing	$\boldsymbol{D}$	=	Difference matrix
P	=	Pressure	$\boldsymbol{Q}$	=	Matrix of eigenvectors
V	=	Internal volume	$\boldsymbol{U}$	=	Matrix of left singular vectors
x, z	=	Cartesian coordinates	$\boldsymbol{V}$	=	Matrix of right singular vectors
γ	=	Ratio of specific heats	$\mathbf{x}$	=	Discrete surface geometry vector
δ	=	Undivided difference	$\boldsymbol{\Lambda}$	=	Matrix of eigenvalues
ϵ	=	Absolute constraint bound	$\boldsymbol{\Sigma}$	=	Matrix of singular values
ρ	=	Density	$\boldsymbol{\phi}$	=	Shape basis matrix
σ	=	Singular value			
μ	=	Length scale constraint parameter			

I. Introduction

Numerical shape optimisation has many applications across aerospace engineering, with optimal design objectives such as aerodynamic drag, structural weight, aeroacoustic signature, mission endurance, electromagnetic stealth as well as various multidisciplinary objectives. A shape optimisation framework comprises three main components: a numerical analysis code; a geometry representation and manipulation method (including mesh deformation); and a numerical optimisation method.

The choice of geometry control has particular influence on the number of optimisation iterations in shape optimisation since it acts as the interface between the search algorithm, which operates on the vector of design variables, and the analysis code, which is only concerned with the geometry. The conditioning of the shape control, which is here defined as that of the geometric Jacobian, is of particular importance since it describes the quality of the mapping between design variables and surface geometry; a poorly conditioned shape basis is one in which small design variable changes produce large shape changes and conversely, shapes that are geometrically similar do not have similar design variable vectors. Whereas a well-conditioned shape parameterisation does little to affect the conditioning of the overall optimisation problem, based on the Hessian of the objective, empirical evidence indicates that a poorly-conditioned

shape parameterisation can have a consequently detrimental effect [1, 2]. Similarly, the ability to arbitrarily refine shape control is highly desirable for shape optimisation, however existing methods often exhibit poor optimisation performance when shape control is refined due to degraded design space conditioning or the generation of non-smooth shapes [3–5]. Without addressing shape smoothness, gradient-based optimisation methods naturally amplify high-frequency shape components which can lead to poor convergence of the optimisation problem, with convergence rate exhibiting dependence on the fidelity of shape-control. This phenomenon was identified in the early work of Drela [6] and Jameson [3], the latter of which applied sensitivity smoothing as a solution.

Previous work by the authors [1, 7, 8] has demonstrated that the problem arises due to the discrete shape problem being ill-posed since it naturally includes geometries that are invalid both in physicality (shape) and discretisation (mesh). In this way the search space not only contains the physical solution(s) but also non-physical solutions, which manifest as non-smooth shapes with wavelength of the numerical grid. The previous work developed a new gradient-limiting approach to shape control using surface gradient constraints to bound the out-of-plane variations for smooth shapes as well as the in-plane variations for mesh validity. This approach was shown to allow high-fidelity control since the surface constraints exclude non-physical shapes from the design space making the shape problem well-posed. In this paper, the same gradient-limiting methodology is further developed by exploiting its linearity to generate orthogonal shape modes.

Orthogonal modes extracted by singular value decomposition (SVD) [9] have been applied to aerofoil optimisation [10] and shown to be highly effective when compared to other shape control methods [5, 11]. However, a notable disadvantage of this method is its dependence on an initial geometry database. Hence, in this paper, the gradient-limiting methodology is developed further and reformulated to produce generic orthogonal geometric shape modes, that do not require a database of training geometry and that possess an equivalent surface smoothness constraint.

The contents of the paper is organised as follows: in the following section background is presented on shape control for aerodynamic optimisation, and the challenges encountered at high-fidelity. In section III the singular value decomposition and its application to deriving compact shape modes is reviewed. In section IV, background motivation for the new generic methodology is presented followed by formulation and practical details. Finally sections VI and VII present the methodology and results for applying the new generic shape modes to drag minimisation using a gradient-based adjoint optimisation framework. Two standard test cases from the AIAA ADODG test suite are tackled including the geometrically challenging and well-studied symmetric transonic aerofoil case. A non-standard multi-body biplane test case is also presented which demonstrates the advantages of a high-fidelity design space and the inclusion of pure translational modes that arise naturally out of the generic modes formulation.

II. Background

Shape control methods

A variety of shape control methods are encountered in aerodynamic shape optimisation including: spline surfaces [12]; volume splines[13–15]; and various other shape functions derived analytically (Hicks-Henne [16] and shape-class functions [17]), from physical considerations (fictitous loads [18]) or numerically (orthogonal modes [9]). All such methods reduce the dimensionality of the continuous shape problem and introduce some smoothing, an advantage that was emphasised by Braibant and Fleury when advocating the use of B-Splines for shape optimisation [12]. However the reduction in dimensionality must be weighed against the need to represent the optimal shape. This trade-off is investigated extensively by Masters *et al.* for several different parameterisation methods [5, 11].

The use of orthogonal modes for shape optimisation follows the reasoning of data reduction which aims to reduce the degrees of freedom of some space while still retaining a suitable approximation to this space within a tolerance. Robinson and Keane [19] derived a set of numerical basis functions by sequential least-squares fitting of a training dataset of nine supercritical aerofoils, these functions were then orthogonalised by the Gram-Schmitt procedure. Toal *et al.* [20] performed POD using eigenanalysis on training data generated artificially by sampling the design space of a NURBS aerofoil representation. Significant work using SVD-based orthogonal aerofoil modes has been done by Poole *et al.* [9, 21] who use an aerodynamic metric to select training aerofoils from a historical database. The SVD approach is applied to aerodynamic shape optimisation [21] used in combination with RBF-FFD for surface and volume mesh deformation. Allen *et al.* [22] applied the same combined SVD-FFD methodology to aerodynamic optimisation of the MDO wing; here the aerofoil modes are applied sectionally along the span to FFD control points which ensure a smooth spanwise blending of the sectional design variables. And in [23] the same methodology is applied to aero-structural optimisation. By contrast Cinquegrana *et al.* [24] generate three-dimensional modes for a wing geometry by perturbing the design variables of a CST parameterisation. Similarly, Ghoman *et al.* [25] generate a snapshot database of 22 wing geometries by manually varying parameters such as taper and sweep.

Shape smoothness and conditioning

As mentioned previously, shape control methods vary in the conditioning of the design space and their ability to generate high-frequency shape components. Without addressing shape smoothness, gradient-based optimisation methods naturally amplify high-frequency shape components, producing non-smooth search directions. The implication for numerical optimisation is that both the search direction is poor and step size severely restricted resulting in slow progress. This problem affects localised shape control methods, such as B-Splines, whereby as the number of design variables increases the shape functions become more localised.

In contrast, for shape functions which exhibit a large zone of influence and remain smooth with refinement, the conditioning of the shape control generally increases significantly as the number of design variables increases. Whereas

local basis functions retain linear independence as they are refined, shape basis functions with large support suffer from deteriorating linear independence such that increasing the number of design variables give diminishing additions to the design space. This means that similar shapes do not have similar control vectors, *i.e.* shapes that are geometrically similar do not lie close together within the design space. This is especially undesirable for gradient-based optimisers which generate a sequence of solutions by stepping through the design space, the effect being that although convergence is generally unaffected by increased control fidelity, the final attainable result of the optimisation is not improved. For example, in [26] high-order Beziers (96 knots) became 'saturated' as the design variables hit their respective upper bounds during optimisation and preventing further improvement.

Recent work by the authors [7, 8] addresses both shape smoothness and design space conditioning explicitly and demonstrates that a sufficiently constrained and well-conditioned design space is all that is required for a well-posed shape optimisation problem without limitation on the attainable design fidelity. In the previous work by the authors, shape gradient constraints approximating a C2 continuity condition for discrete mesh points and cubic B-Spline curves were derived, and demonstrated on a standard test case. The resulting shape optimisation problem is well-posed, as the design space is sufficiently bounded, and well-conditioned since local control methods (mesh-points and B-Splines) are used. The local control methods with two-dimensional (x,z) control provide high-fidelity shape-relevant control, whereas the surface constraints exclude non-physical shapes from the design space. The gradient-limiting methodology was tested on a standard aerodynamic optimisation test case defined by the AIAA aerodynamic design optimisation discussion group. A value of 1.6 drag counts was achieved on the NACA0012 inviscid case; the lowest results published for this case to the authors' knowledge. Significantly, the regularised shape problem is shown to have an optimisation convergence rate independent of shape control fidelity when using B-Splines, while still making use of increased control fidelity to achieve improved results. As a result, high-fidelity shape optimisation is possible at a reasonable computational cost.

A significant development on the gradient limiting methodology is presented in this work, whereby the linear gradient constraints are used to derive generic orthogonal shape modes and design variable bounds are shown to maintain surface smoothness in the same way. This formulation removes the requirement for a large number of linear constraints and generalises the orthogonal modes concept to arbitrary shape optimisation problems.

III. Singular Value Decomposition

In this section, theory is first presented on the singular value decomposition, followed by how it can be used to generate orthogonal shape modes for aerodynamic optimisation.

A. Formulation

The singular value decomposition of an $m \times n$ matrix $\boldsymbol{A}$ is a factorisation thereof into two orthonormal matrices $\boldsymbol{U}$ and $\boldsymbol{V}$, and a diagonal matrix Σ:

$$\boldsymbol{A} = \boldsymbol{U}\boldsymbol{\Sigma}\boldsymbol{V}^T \tag{1}$$

Matrix $\boldsymbol{U}$ is of dimension $m \times m$, the columns of which comprise the *left singular vectors*. Similarly, matrix $\boldsymbol{V}$ is of dimension $n \times n$ and contains the *right singular vectors*. The diagonal matrix $\boldsymbol{\Sigma}$ is of dimension $m \times n$, and contains the singular values σ_i along the diagonal. The number of singular values is therefore the smaller of m, n for an $m \times n$ matrix. It is customary for singular values to be arranged in order of decreasing magnitude, with the singular vectors ordered correspondingly.

In generating an orthogonal modal basis with a corresponding diagonal matrix, the SVD resembles the eigendecomposition:

$$\boldsymbol{A} = \boldsymbol{Q}\boldsymbol{\Lambda}\boldsymbol{Q}^T \tag{2}$$

with eigenvectors $\boldsymbol{q}_j$ and eigenvalues Λ_{ii}. The SVD can be viewed as a generalisation of the eigendecomposition since it is applicable to both square and non-square matrices and the two are related in that the left singular values $\boldsymbol{U}$ are the eigenvectors of $\boldsymbol{A}\boldsymbol{A}^T$ and the singular values σ_i are the square roots of the eigenvalues of $\boldsymbol{A}\boldsymbol{A}^T$.

Since the SVD is calculated numerically (at a cost of $O(mn^2)$ operations), with finite precision arithmetic, a *numerical rank* can be defined by specifying some cut-off tolerance for identifying the vanishing singular values. If $\boldsymbol{A}$ is not of full rank (rank $r < \min[m, n]$), then the there will be $(\min[m, n] - r)$ vanishing singular values where the corresponding right singular vectors span the null space of the matrix. Likewise, the left singular vectors corresponding to the non-vanishing singular values represent the range of the matrix $\boldsymbol{A}$, and can therefore be used as a basis. Moreover, since the SVD extracts the dominant features of the matrix, indicated by the magnitude of the respective singular values, then an efficient reduced-order basis can be constructed from $\boldsymbol{U}$ simply by truncating the basis. The basis is efficient in the sense that, if formed of the first k modes, it is the best approximation of rank k to the original matrix as measured by the Frobenius norm [27].

B. Orthogonal Shape Modes

To demonstrate the SVD method, a library-based decomposition was first produced. The normalised aerofoil library of Masters *et al.* [11] provides a large database of 1300 aerofoils* all defined by 301 points. Since all the aerofoils have a common x distribution, only the z-ordinate (thickness) is used for modal analysis. The matrix $\boldsymbol{A}$ is then constructed

*Database available as supplementary material at: https://arc.aiaa.org/doi/suppl/10.2514/1.J054943 (accessed November 2019)

simply by horizontal concatenation of the aerofoil z-ordinates:

$$\boldsymbol{A} = \begin{pmatrix} z_{1,1} & z_{2,1} & \cdots & z_{n,1} \\ \vdots & & \ddots & \vdots \\ z_{1,m} & z_{2,m} & \cdots & z_{n,m} \end{pmatrix} \tag{3}$$

where $z_{i,j}$ is the j^{th} z-ordinate of the i^{th} aerofoil. Taking the SVD of this matrix (equation 1) gives the orthogonal shape modes contained in the left singular matrix $\boldsymbol{U}$ and their relative importance within the library in the singular value matrix $\boldsymbol{\Sigma}$. Figures 1(b) and 1(a) show the singular values and first six normalised singular vectors produced from singular value decomposition of the aerofoil library where each aerofoil consists of $N = 301$ points.

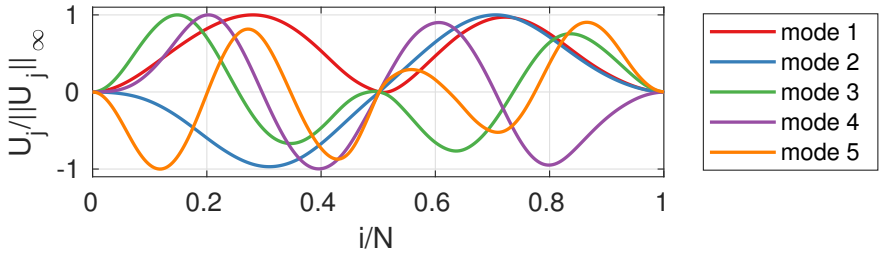

(a) First five singular vectors

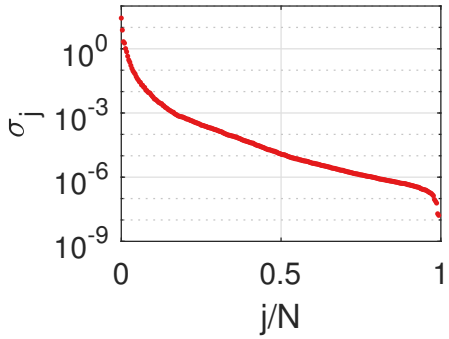

(b) Singular values

Fig. 1 Singular value decomposition of an aerofoil library

Note the initial rapid drop in singular values indicating the greater importance of the first 50 or so modes compared to the remainder. Also note the last singular value is machine zero, indicating that the rank of the matrix A is less than its row dimension defined by the number of points discretising each aerofoil; this can be attributed to the repeated trailing edge point giving redundancy. The singular vectors resemble oscillatory modes with fixed points at the leading and trailing edges due to the library normalisation. As one progresses through the singular vectors, the wave number of the mode increases corresponding to increasing shape resolution.

C. Design Variables for Optimisation

There are two important benefits of using orthogonal modes from SVD as a basis for shape optimisation: first, the shape control basis is guaranteed to be perfectly conditioned (condition number of one) since the basis is orthonormal. This ensures that the shape parameterisation does not adversely affect the conditioning of the overall shape optimisation problem which, as previously discussed, has been shown to be influenced by poorly-conditioned shape parameterisations [1, 2]. However, it is emphasised that a well-conditioned shape parameterisation is no guarantee of a well-conditioned shape optimisation problem. The second benefit is that a shape basis of arbitrary fidelity (number of design variables) can be chosen by truncating the orthogonal basis. In the case of orthogonal modes generated from an aerofoil library described above, the truncated basis is guaranteed to be the most efficient geometric representation for that number of design variables [9, 11].

Once a set, or truncated subset, of the singular vectors has been generated, these can be used as a basis $\boldsymbol{\phi}$ for shape parameterisation. There are two standard approaches to parameterising shapes with a set of basis functions:

1) **Constructive:** Shapes are defined entirely by the basis:

$$\mathbf{x}(\boldsymbol{\alpha}) = \sum_{j=1}^{N} \boldsymbol{\phi_j} \alpha_j \tag{4}$$

2) **Deformative:** Shapes are defined by perturbations to an initial geometry where only the perturbations belong to the basis:

$$\mathbf{x}(\boldsymbol{\alpha}) = \mathbf{x}^0 + \sum_{j=1}^{N} \boldsymbol{\phi_j} \alpha_j \tag{5}$$

The primary advantage of the deformative approach occurs when the initial geometry $\mathbf{x}^0$ cannot be accurately represented by the basis $\boldsymbol{\phi}$; this is often the case since the shape basis is ideally compact for shape optimisation whereas the input geometry may be arbitrarily complex. Hence the deformative method gives better flexibility for different problem types compared to the constructive approach which is constrained to geometry that can be represented by the basis. A third approach exists [28] whereby the basis $\boldsymbol{\phi}$ is augmented with those components of $\mathbf{x}^0$ not belonging to the basis, thus converting the deformative formulation to a constructive one while retaining representation of the initial geometry; this is advantageous when the input geometry may contain undesirable numerical features.

Shape basis functions derived from SVD can be used as either a constructive or deformative basis; in this work, the deformative formulation (equation 5) is used, without loss of generality, where the basis $\boldsymbol{\phi}$ is formed of a truncated set of orthogonal modes and the initial geometry $\mathbf{x}^0$ is the NACA 0012 aerofoil. Figure 2 shows these orthogonal library-based modes, applied as perturbations to the NACA 0012 aerofoil. Here it is much clearer how the SVD method can extract the fundamental features from the aerofoil library using a combination of symmetric and non-symmetric modes which can be interpreted as perturbations to thickness and camber respectively. The first two modes are recognisable as

fundamental camber and thickness modes, and as the wave number increases in subsequent modes shorter wavelength modifications are available. As can be expected, mode shapes generated in this manner from a geometry library can

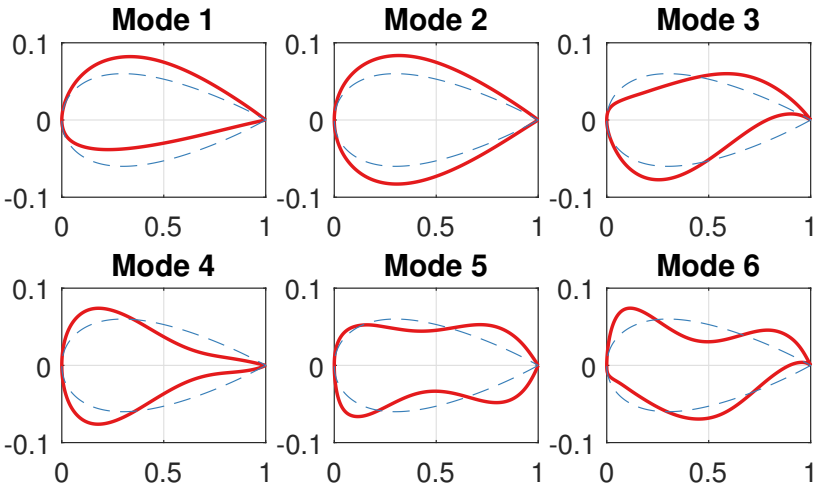

Fig. 2 Library-based mode shapes applied to NACA0012 aerofoil

represent similar geometry very accurately using few fundamental modes. However, this methodology is heavily reliant on the existence of a database of representative geometry which is unlikely to exist for general problems. Even when a geometry database exists, or is constructed artificially, the resulting numerical modes are dependent on which geometry is present in the database and how that geometry has been parameterised and normalised. These limitations restrict the application of orthogonal mode shapes to arbitrary problems, particularly those involving surfaces in three dimensions. In the following section, an alternative derivation of orthogonal modes is presented which does not require a geometry database and hence is not restricted in the same way.

IV. Generic Modal Design Variables

The objective of the work here is to reformulate the gradient-limiting methodology to produce completely generic design variables applicable to arbitrary shape optimisation problems. The approach developed has two significant advantages: the large number of linear constraints in the gradient-limiting method are replaced by simple bound constraints; and universal orthogonal modes can be produced that are completely independent of geometry. The methodology for deriving the universal modal design variables is given in this section, starting with a brief description of the original gradient-limiting method.

A. Shape gradient constraints

A gradient-limiting methodology has been developed by the authors [7, 8] to control smoothness during shape optimisation; this is done by applying a linear constraint to the design variables which bounds the third derivative as approximated by undivided differences or spline derivatives. Given a shape control basis $\boldsymbol{\phi}$, derived from a local shape control method such as grid-point control or cubic B-Spine, the discretised geometry $\mathbf{x}$ for analysis is given by:

$$\mathbf{x} = \boldsymbol{\phi}\boldsymbol{\alpha} \tag{6}$$

where $\boldsymbol{\alpha}$ is the vector of design variables. The gradient-limiting methodology is implemented as a linear constraint:

$$-\boldsymbol{\epsilon} \leq \boldsymbol{D}\mathbf{x} \leq \boldsymbol{\epsilon} \tag{7}$$

where $\boldsymbol{D}$ implements some form of discrete difference operator for a given order of smoothness. For example, an approximate C^2 condition is implemented using undivided third differences of grid point vertices or of spline derivatives; for grid points on a simple periodic domain this takes the form:

$$\boldsymbol{D} = \begin{pmatrix} -1 & 3 & -3 & 1 & & & \\ & -1 & 3 & -3 & 1 & & \\ & & \ddots & & & & \\ & & & \ddots & & & \\ & & & & \ddots & & \\ 3 & -3 & 1 & & & & -1 \end{pmatrix} \tag{8}$$

Undivided differences are used since, as shown in [1], this leads to a formulation that enforces in-plane continuity for the discretisation as well as out-of-plane smoothness for the shape. The equivalent using splines involves differences of

spline control points weighted by the spline basis derivatives.

ϵ is the constraint bound, which is expressed as:

$$\epsilon = \mu \bar{h}^3 \tag{9}$$

where $\bar{h}$ is the mean grid spacing distance and μ is the dimensionless constraint parameter with typical values in the range $50 - 200$. Smaller values of μ correspond to enforcing higher shape smoothness with a smaller overall design space, and *vice versa* for larger values. Previous work [1, 7, 8] has shown this approximate C^2 condition ensures surface smoothness and mesh validity during shape optimisation which reduce the effective degrees of freedom in a geometrically meaningful manner and thereby resulting in better optimisation performance.

Whereas the gradient-limiting methodology allows for a well-defined design space, this effectively comes at the cost of increased conditioning of the search-direction subproblem (when using SQP) since the gradient constraint is poorly conditioned. For small-medium problems this is desirable since solution of the quadratic subproblem, even when poorly conditioned, is faster and more robust than optimising in a poorly-conditioned design space due to the high cost of objective function (and gradient) evaluations. However for very large problems the number of gradient constraints required is likely to cause the subproblems to be ill-conditioned.

The motivation for the work here is to exploit the linearity of the gradient constraints to transform the constrained design space into one in which only bound constraints on the individual design variables are required. The resulting problem will have no linear constraints and will hence not restrict the choice of search algorithm. This extends the technique to application with global gradient-free search methods and importantly the method will be scalable to larger more complex geometries in three-dimensions.

B. Gradient-limiting orthogonal modes

The undivided differences $\boldsymbol{\delta}$, which are the gradient terms to be subject to linear constraints (equation 7), are given by:

$$\boldsymbol{\delta} = \boldsymbol{D}\mathbf{x} = \boldsymbol{D}\boldsymbol{\phi}\boldsymbol{\alpha} \tag{10}$$

One approach to removing the linear constraints would be to adopt the inverse, or pseudo-inverse, of the differencing matrix as the shape control basis:

$$\boldsymbol{\phi} = \boldsymbol{D}^{-1} \tag{11}$$

such that $\boldsymbol{\delta} = \boldsymbol{\alpha}$, *i.e.* the design variables directly specify the surface differences. This would effectively give an *implicit* surface defined as that which satisfies the surface derivatives specified by the design variables. However, for the approximate C^2 condition, a quad-diagonal third-difference matrix is required the condition number of which grows with the cube of its dimension.

An alternative to the difference matrix inverse, which will be used here, is to factorise the difference matrix using the singular value decomposition (SVD) of the difference matrix. Taking the SVD of the differencing matrix yields:

$$\boldsymbol{D} = \boldsymbol{U}\boldsymbol{\Sigma}\boldsymbol{V}^T \tag{12}$$

Choosing the shape control basis from the right singular vectors, $\boldsymbol{\phi} = \boldsymbol{V}$, leads to the following reformulation of the undivided differences:

$$\boldsymbol{\delta} = \boldsymbol{D}\boldsymbol{V}\boldsymbol{\alpha} \tag{13}$$

which, after substituting the decomposition of $\boldsymbol{D}$, becomes:

$$\boldsymbol{\delta} = \boldsymbol{U}\boldsymbol{\Sigma}\boldsymbol{V}^T\boldsymbol{V}\boldsymbol{\alpha} \tag{14}$$

and then simplifying by orthonormality of $\boldsymbol{V}$ gives:

$$\boldsymbol{\delta} = \boldsymbol{U}\boldsymbol{\Sigma}\boldsymbol{\alpha} \tag{15}$$

Hence the left singular vectors $\boldsymbol{U}$ are the normalised third differences of each mode given in $\boldsymbol{V}$ where the magnitude of the third differences are modulated by the corresponding singular value in $\boldsymbol{\Sigma}$. *i.e.* the singular value σ_j gives a measure of the 'non-smoothness' of the orthogonal mode $\boldsymbol{V_j}$.

Consider one row i from this expression, which represents the gradient constraint at a single location on the geometry:

$$\delta_i = \sum_{j=1}^{m} u_{ij}\sigma_j\alpha_j \tag{16}$$

From this expression it is clear that the contribution of a specific mode α_j, from the new modal basis $\boldsymbol{\phi} = \boldsymbol{V}$, to the constraint i is governed by its corresponding singular value σ_j such that if the design variables satisfy some reciprocal function of the singular values, then upper bounds may be placed on δ_i:

$$|\alpha_j| \leq \frac{\epsilon}{f(\sigma_j)} \tag{17}$$

Note that whereas this condition is not equivalent to the original gradient-limiting linear constraint, a good approximation can be made via an upper bound since the singular vectors $\boldsymbol{U}$ are orthonormal. This is the motivation for deriving shape modes from the differencing matrix $\boldsymbol{D}$: bounds can be placed on the design variables that emulate the gradient-limiting methodology to reduce the design space in a geometrically meaningful way by enforcing shape smoothness. The formulation of such design variable bounds is presented in the next section as applied to aerofoils. In the remainder

of this section, examples are given on a simple 1D periodic domain demonstrating the equivalency with Laplacian eigenfunctions and the enforcement of useful geometric boundary conditions.

C. Example on a periodic domain

The simplest example is that of a one-dimensional discrete curve on a periodic domain discretised into N piecewise linear segments. In this case the third difference matrix, required for approximate C^2 continuity, can be formed by repeated application of the circulent first difference matrix $\boldsymbol{D_1}$:

$$\boldsymbol{D_1} = \begin{pmatrix} -1 & 1 & & \\ & -1 & 1 & \\ & & \ddots & \\ 1 & & & -1 \end{pmatrix} \tag{18}$$

The second are therefore:

$$\boldsymbol{D_2} = \boldsymbol{D_1}^T \boldsymbol{D_1} \tag{19}$$

where the transpose product is used since $\boldsymbol{D_1}$ maps from nodal values to element values and *vice versa.* Similarly, the third differences are:

$$\boldsymbol{D_3} = \boldsymbol{D_1} \boldsymbol{D_2} \tag{20}$$

The matrices $\boldsymbol{D_1}$,$\boldsymbol{D_2}$ and $\boldsymbol{D_3}$ are all dimension $N \times N$ where the first and third differences are associated with each of the N elements and the second differences are associated with the N nodes. Since the domain is periodic the $(N+1)$ node is identical to the first node.

Considering now the singular value decomposition of the first difference matrix $\boldsymbol{D_1}$:

$$\boldsymbol{D_1} = \boldsymbol{U}\boldsymbol{\Sigma}\boldsymbol{V}^T \tag{21}$$

then, due to orthonormality of $\boldsymbol{U}$, the second difference matrix is:

$$\begin{aligned} \boldsymbol{D_2} =& (\boldsymbol{U}\boldsymbol{\Sigma}\boldsymbol{V}^T)^T \boldsymbol{U}\boldsymbol{\Sigma}\boldsymbol{V}^T \\ & \boldsymbol{V}\boldsymbol{\Sigma}^T\boldsymbol{U}^T\boldsymbol{U}\boldsymbol{\Sigma}\boldsymbol{V}^T \\ & \boldsymbol{V}(\boldsymbol{\Sigma}^T\boldsymbol{\Sigma})\boldsymbol{V}^T \end{aligned} \tag{22}$$

and similarly the third differences:

$$\boldsymbol{D_3} = \boldsymbol{U}(\boldsymbol{\Sigma}\boldsymbol{\Sigma}^T\boldsymbol{\Sigma})\boldsymbol{V}^T \tag{23}$$

Therefore for the periodic case, the singular vectors of the first and third differences are identical and since $\mathbf{\Sigma}$ is diagonal, the singular values are simply powers of the first difference values. Furthermore, the right-singular vectors $\boldsymbol{V}$ of the first and third differences are the eigenvectors of the second difference matrix; these are known as the *Laplacian eigenvectors*.

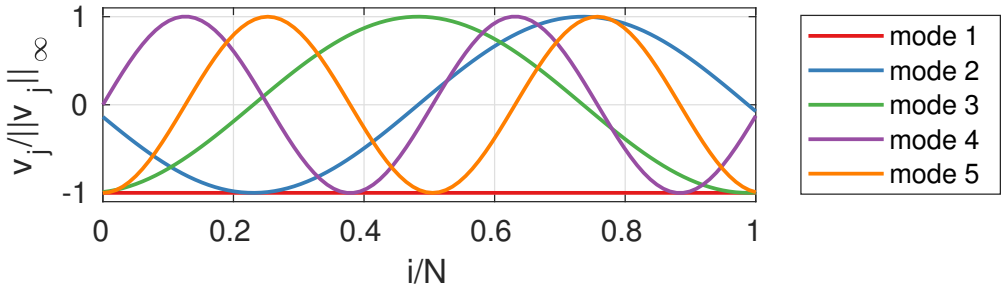

(a) Five Laplacian eigenvectors (normalised magnitude)

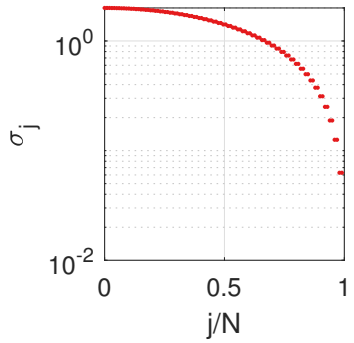

(b) Singular values

Fig. 3 Laplacian eigenmodes from undivided differences on a periodic domain

Figure 3(a) shows the first five modes for the periodic case considered here. In this and subsequent plots, the modes are normalised by maximum amplitude. Since the difference matrices are circulent for this simple periodic case, the resulting modes are just the Fourier modes. Physically, they may be interpreted as the sinusoidal vibrational modes of an unconstrained infinite uniform string. Note also the inclusion of a purely constant mode corresponding to a rigid body mode. Therefore, one way to interpret the singular vectors of undivided differences are as pseudo-structural modes. Figure 3(b) shows the corresponding singular values. As the wave number of the mode increases the corresponding singular value increases indicating a reduction in 'smoothness' of the mode as measured by the discrete difference operator.

A significant advantage of shape modes derived in this manner is that they are dependent only on the connective topology of the shape as defined by the terms of the difference matrix. Connective topology here refers to the connectivity of elements as well as the presence of discrete features such as sharp points and edges which occur as boundary conditions within the difference stencil. Significantly, and unlike most applications of proper orthogonal decomposition, no database of training data is required—this extends the technique to a wider variety of unique shape problems

particularly in three-dimensions. The application of the method in three-dimensions only requires defining a suitable difference operator for the surface geometry such as using a uniform mesh Laplacian or differences along iso-parametric lines. The ordering of modes in the three dimensional case may require additional consideration since the wave number can vary in more than one dimension, however for a suitable difference operator the modes are still expected to be ordered by increasing frequency in some sense. The discussion of such surface operators is beyond the scope of this paper, but importantly there is no fundamental limitation on the choice of difference operator used to generate modes for shape control.

The use of undivided differences here allows for consistency with the previous gradient-limiting approach. An unintuitive advantage of using undivided differences, which is found to be useful for the test cases demonstrated later, is that it naturally localises the basis functions in physical space at areas of high mesh density. Hence, more local control is automatically achieved in areas where the flow or geometry are more complex. Moreover, the nature of the mode shapes in the limit of mesh refinement is unaffected since such refinement only adds to the number of higher frequency modes which are typically not used for shape control due to truncation of the basis. There is, however, no limitation on the form of differences used and mesh-dependent differences may also be used to produce mesh-independent mode shapes.

An advantage of the Laplacian eigenfunctions generated in this manner is that they are tailored to the shape and boundary conditions of the particular domain; for example, rectangular domains give rise to sines and cosines, spherical domains give the spherical harmonics and on a cylinder they are Bessel functions. This is particularly advantageous for three-dimensional shape optimisation in which a wide variety of possible topologies are possible. Moreover, this methodology naturally produces a pure translational mode, or an equivalent set of piecewise linear modes depending on the boundary conditions used, while retaining an orthogonal basis.

In this work, the Laplacian eigenfunctions are not calculated by eigen-decomposition of the Laplacian, but instead equivalent modes are extracted using singular value decomposition of the third difference matrix since this gives greater flexibility for enforcing geometric boundary conditions while retaining orthogonality in the resulting basis.

In the remainder of this section, two important boundary conditions are considered:

1) **Sharp condition**

2) **Interpolating condition**

D. Sharp condition

The sharp condition allows points to be specified with zero-order continuity only (connectedness). This is particularly useful for sharp features such as trailing edges, but generalises to surface creases and features in 3D. The sharp condition is formulated by modifying the difference scheme around specified points such that the second difference at such points always evaluates to zero. This corresponds to setting the i^{th} row of $\boldsymbol{D_2}$ to zero.

Modifying the simple periodic example presented previously such that the central point is sharp gives the basis

functions shown in Figure 4. The basis functions are now no longer simple sinusoids, but more complex where continuity reduces to C^0 at the central point for those modes that are anti-nodal there. Application of the $\boldsymbol{D_2}$ difference operator on these modes verifies that the parametric curvature, measured by the second differences, is zero at the sharp point.

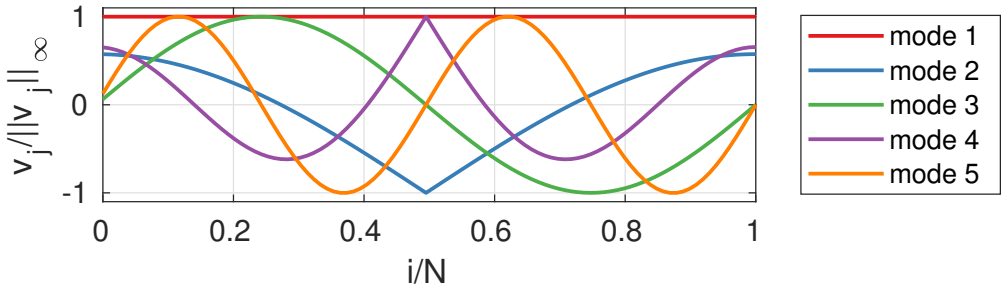

Fig. 4 First five generic modes (normalised) with a sharp condition

When the sharp condition is specified at $n > 1$ points, then the rigid body mode is replaced by n piecewise linear modes as shown in Figure 5. Note that rigid body motion is still possible using a weighted combination of the piecewise linear modes.

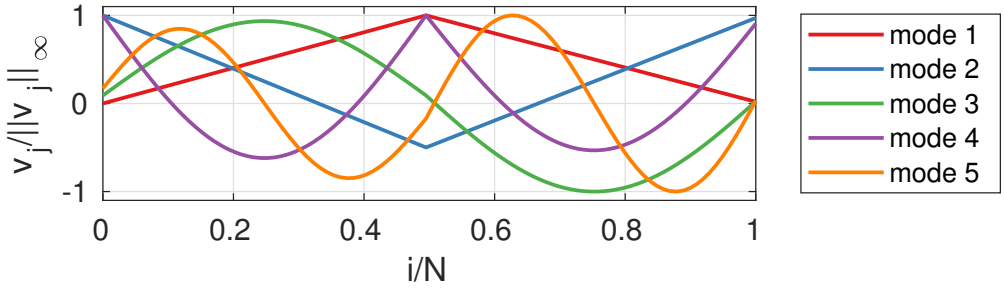

Fig. 5 First five generic modes (normalised) with two sharp points

E. Interpolating Condition

When the modal basis is used to parameterise perturbations to an initial geometry (deformative parameterisation, equation 5) it can be useful to specify locations on the initial geometry that should remain unperturbed. This can be used for constraining geometry features such as a wing root section or leading and trailing edge locations.

To interpolate the discrete point with index i, the third difference matrix $\boldsymbol{D_3}$ is modified such that the cartesian unit vector $\boldsymbol{e_i}$ lies within the null space of $\boldsymbol{D_3}$. This is achieved trivially by replacing the i^{th} column in $\boldsymbol{D_3}$ with the zero vector. The cartesian unit vector replaces the rigid body mode in the null-space of $\boldsymbol{D_3}$ however it is not included in the generic modal basis since the role of the rigid body mode is fulfilled by the initial geometry $\mathbf{x}^0$ when parameterising perturbations.

Again modifying the simple periodic example now such that the central point is interpolating yields the basis functions shown in Figure 6. Note that all modes now pass through zero at the central point such that this point remains

unperturbed by the basis.

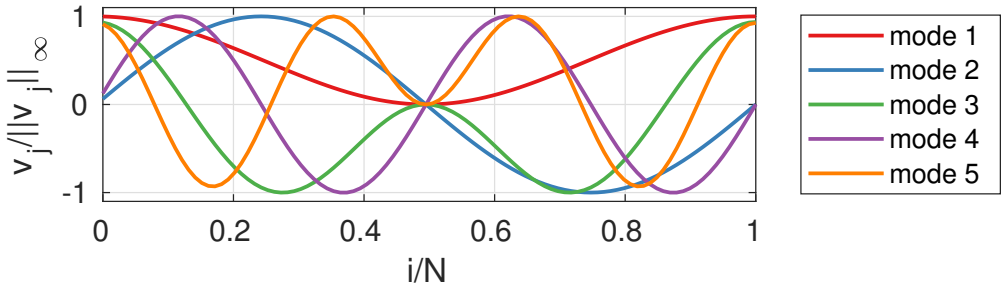

Fig. 6 Generic modes with an interpolating condition

Finally, Figure 7 shows the resulting basis functions when combining the sharp condition with the interpolating condition at the central point. As in Figure 6, all modes pass through zero at the central point, however now modes one, three and five, which are anti-nodal at the central point, see a reduction in continuity such that this point is always sharp in the new basis.

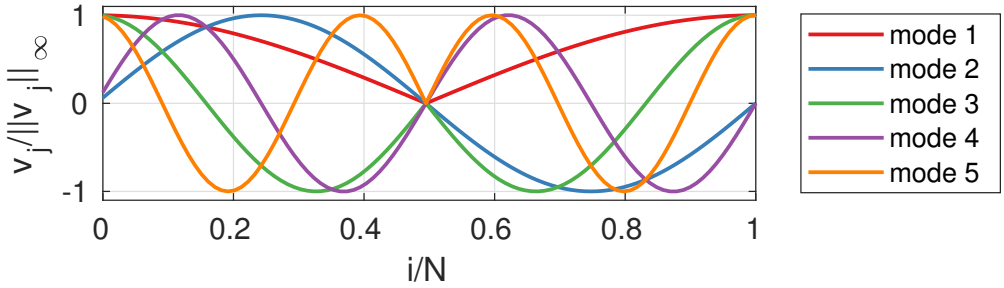

Fig. 7 Generic modes with a sharp interpolating condition

V. Orthogonal Modes for Optimisation

In this section, detail is given on how the generic modal basis derived previously can be applied to aerodynamic shape optimisation. The resulting design variables are assessed by demonstrating geometric shape recovery of a library of aerofoils. Finally design variable bounds are formulated using the singular values in order to emulate the gradient-limiting methodology and thereby ensure a well-posed optimisation problem.

A. Implementation

To generate orthogonal modes for aerodynamic shape optimisation, the third difference matrix is first constructed for the particular geometry; this can be done using the individual grid points or by using a spline approximation and using the spline derivatives. To exploit the interpolating condition for the leading and trailing edges, generic modes are used in a deformative parameterisation where aerofoils are constructed from perturbations to the NACA 0012 aerofoil. For the aerofoil topology studied in this work the difference matrix is constructed for the individual points of the aerofoil surface

grid and interpolating conditions are used for the leading and trailing edge points with an additional sharp condition at the trailing edge also. Figure 8 shows the resulting modes where grid points are enumerated counter-clockwise starting from the trailing edge such that the leading edge point is at half-way. Note the presence of C^2 continuity around the leading edge but not at the trailing edge.

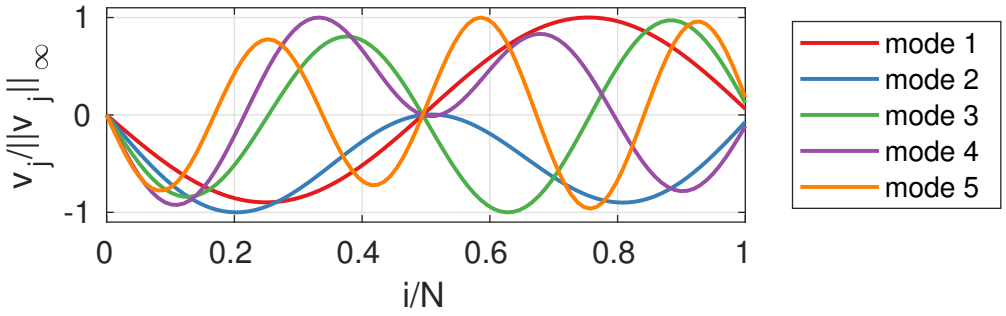

Fig. 8 Generic modes for the aerofoil topology

Plotting the generic modes as perturbations to the NACA 0012 aerofoil, shown in Figure 9, there is a clear resemblance to orthogonal modes derived from the aerofoil library (Figure 2) where there is a general increase in wave number and a combination of symmetric and non-symmetric mode shapes.

The first mode has the longest wavelength and hence lowest singular value (highest parametric smoothness); this mode can be clearly interpreted as a general symmetric thickness mode. Similarly, the mode two resembles a general camber mode with subsequent modes increasing in wave number.

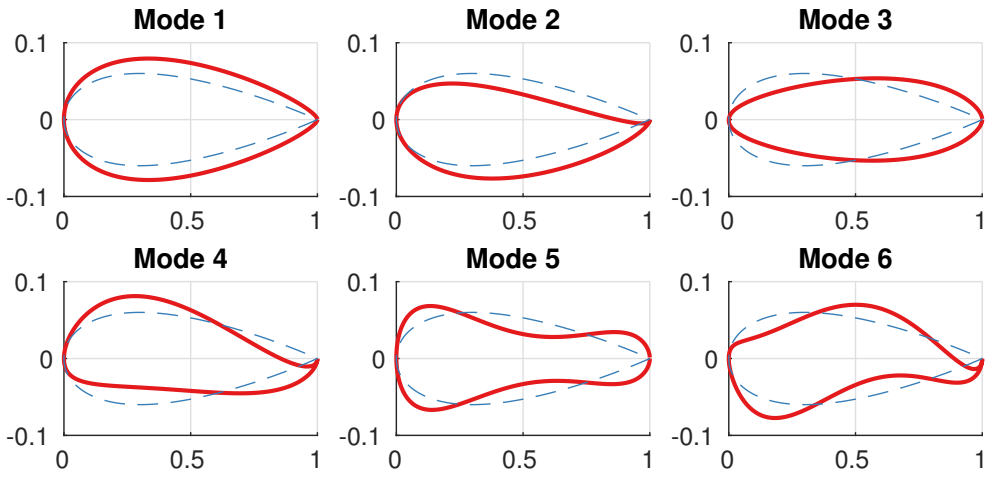

Fig. 9 Generic aerofoil modes shown as displacements to the NACA0012 aerofoil

B. Design Space Coverage

As with other such decompositions, the modal basis generated with this formulation can be truncated to form a compact representation of the original space. This is particularly advantageous for shape optimisation which can have a high dimension search space. For the methodology presented here, it is the last m modes that are extracted from $\boldsymbol{V}$, assuming the usual convention of ordering the SVD basis by decreasing singular value magnitude. This is because the methodology essentially seeks to maximise smoothness in the reduced basis and hence modes are chosen in order of increasing singular value. Therefore modes are enumerated starting from the 'smoothest' mode in the last column vector of $\boldsymbol{V}$ (mode 1).

To assess the suitability of the resulting generic modes for aerodynamic shape optimisation, a large database test is performed in which a library of over 1000 aerofoils is matched using a varying number of modes. The same library as in section III.B is used here for shape matching.

A least squares fit is used to match the aerofoil thickness distribution using the SVD basis and the maximum error is checked against Kulfan's tolerance (8×10^{-4}) [29]. Only the thickness distribution (z ordinate) is matched in these tests since all aerofoils in the database used here have the same horizontal (x) point distribution. The fitting procedure is performed using modes derived from both the aerofoil library (section III.B), shown previously in Figure 2, and modes derived using the new generic approach. In both cases, the least-squares fitting procedure only requires a transpose matrix product since the modal basis is orthonormal. In this first section, note that the fitting procedure for the generic modes is unconstrained; it does not include the design variable bounds derived in section IV.B.

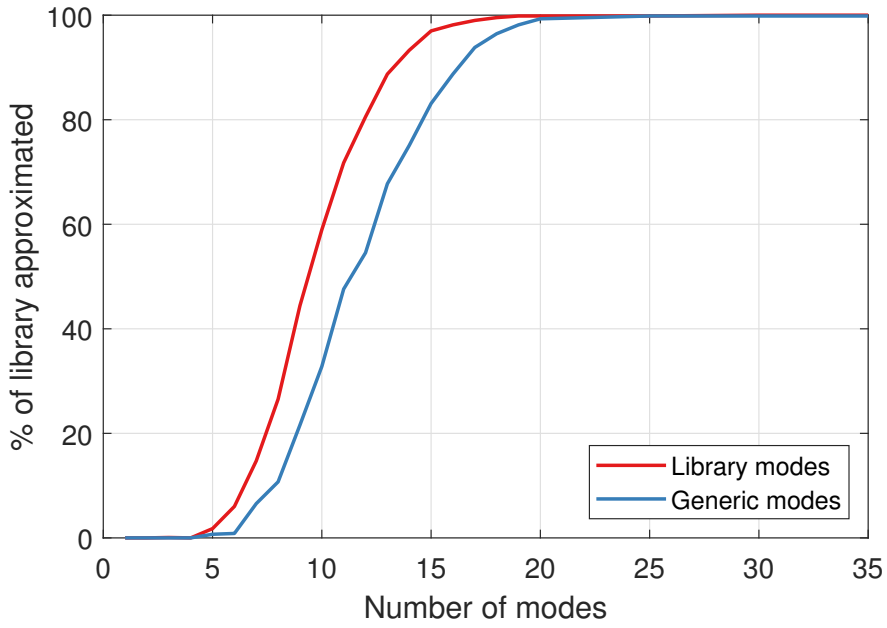

Fig. 10 Recovery of an aerofoil library using varying numbers of orthogonal modes

Figure 10 shows the percentage of library aerofoils that were matched to Kulfan's tolerance for increasing number of

SVD basis modes using orthogonal modes derived from both methods. Orthogonal modes generated by both methods are able to recover the entire library with at least 25 modes. The modes generated from the library perform better overall than modes generated from differences in that fewer such modes are required for equivalent accuracy. This is expected since these modes are generated directly from the library and hence represent the most compact representation thereof. Importantly, the modes generated from differences perform comparable well considering they represent only connectivity information for the aerofoil surface. 90% of the library is represented within Kulfan's tolerance using 20 gradient-limiting modes and 17 library modes.

These results represent the coverage performance of the modes without any form of modal filtering by design variable bounds. In the next section, design space coverage for the new generic modes is investigated under the design variable constraints proposed in section IV.B with the goal to demonstrate the effect of the constraint bound magnitude and give an indication of a suitable range of values.

C. Design Variable Bounds

The motivation for deriving orthogonal design variables from a differencing operator is to enforce some form of gradient-limiting methodology which seeks to ensure a well-posed optimisation problem by reducing the design space in a geometrically meaningful way.

In this work, gradient-limiting design variable bounds (equation 17) are approximated using a simple reciprocal relation with the singular values of the third difference matrix:

$$|\alpha_j| \leq \frac{\epsilon}{\sigma_j} \tag{24}$$

The singular values, derived from a third difference operator, represent the degree of 'non-smoothness' in a particular mode as measured by the same difference operator; hence non-smooth modes with higher singular values are constrained more than smooth modes with low singular values. Alternatively, these variable bounds can be viewed as constraining the total shape 'energy' as specified by the singular values. Importantly these bound constraints are much easier to handle than the linear constraints of the original gradient-limiting approach, thereby placing no restriction on the type of search algorithm to be used.

As with the original gradient-limiting approach, ϵ is defined by a dimensionless parameter μ:

$$\epsilon = \mu \bar{h}^3 \tag{25}$$

where $\bar{h}$ is the mean grid spacing distance. Smaller values of μ correspond to enforcing higher shape smoothness with a smaller overall design space, and *vice versa* for larger values.

A suitable range of values for the parameter μ can be determined using the same aerofoil library and the least-squares fitting presented in the previous section. However in this section, the focus is on the effect of the constraint parameter μ and finding values thereof for which design space coverage is not negatively impacted. A suitable value for μ is the smallest such value that permits the length scales of interest for the shape optimisation problem while excluding all spurious length scales smaller than this. By performing a sweep in μ across a library of historic aerofoils, the aerofoil length scale of interest can be easily determined in terms of the length scale parameter.

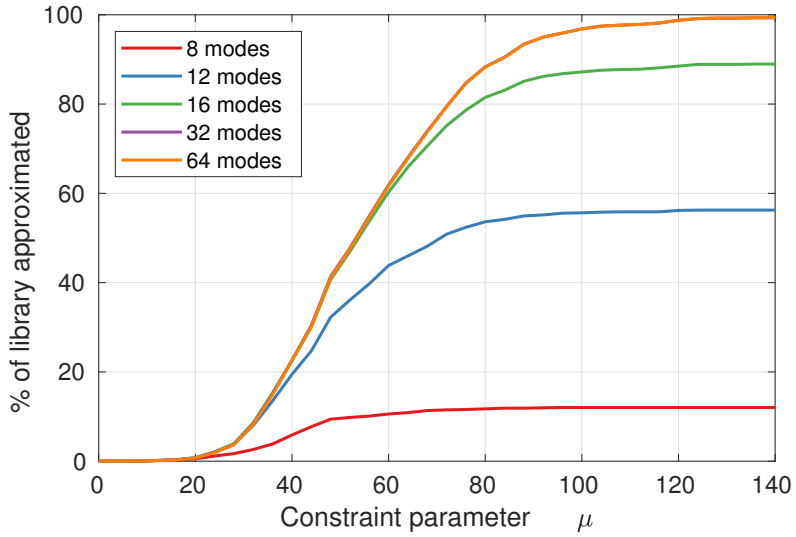

Fig. 11 Recovery of an aerofoil library for varying values of the constraint parameter

Figure 11 shows the percentage of library aerofoils for which the least-squares fit using generic modes satisfies the bound constraint (equation 24) for varying values of the constraint parameter μ and varying number of modes used. Here it is clear that the number of representable aerofoils is dependent on the number of modes in the basis, as shown in the previous section, as well as the value of the constraint parameter. As expected, small values of the constraint parameter, corresponding to a tighter smoothness condition, restrict how many aerofoils can be represented within the generic modal design space. As the constraint parameter is loosened (increased) the number of aerofoils within the constrained design space increases, where in the limit of $\mu \to \infty$ each design fidelity curve tends to the corresponding value in Figure 10 for the unconstrained case. At a value of $\mu \geq 150$, all aerofoils can be represented within tolerance when using at least 20 modes.

VI. Optimisation Methodology

In this section, detail is given on the tools and methods used for the aerodynamic shape optimisation test cases presented in the next section.

A. Flow solver: SU2

For this work the Stanford University Unstructured (SU^2) [30] flow solver is adopted. This open-source software was constructed with aerodynamic shape optimisation in mind and hence has both continuous and discrete adjoint implementations [31]. The main flow solver implements both the compressible Euler and RANS equations using an unstructured finite volume method. For those test cases requiring the RANS equations, the one equation Spalart Allmaras turbulence model [32] is used as implemented in SU^2.

Multigrid acceleration is available as well as MPI parallel processing. The SU^2 suite also includes other modules for tasks such as shape parameterisation, mesh adaption and mesh deformation, however only the CFD module with continuous adjoint is used here for obtaining flow solutions and objective sensitivities. During optimisation, the primal and adjoint solutions are converged down to an absolute residual of 10^{-8} on density (and corresponding dual), except in cases where the primal has restarted from a previous solution when a tighter tolerance of 10^{-10} is used.

B. Volume mesh handling

High quality structured meshes are are generated here by a conformal mapping approach, with an orthogonality smoothing algorithm. O-meshes are used for inviscid cases, and C-meshes for viscous cases. Figure 12 shows the coarse viscous mesh used for the RAE2822 case, and Figure 15 shows three views of the complete 513×257 mesh, used for the NACA0012 case; the leading and trailing edge images have the same window size and Figure 15(a) shows every other point in each direction for clarity. During shape optimisation, mesh deformation is used to produce new meshes for the displaced surface geometry from the initial volume mesh. Not only is this computationally cheaper than regenerating a mesh for each geometry iteration but it also maintains consistency of the discretisation error which is highly desirable during iterative numerical optimisation.

In this work interpolation using multiscale radial basis functions (RBFs) [33] is used. Interpolation using radial basis functions (RBFs) has recently become a prominent mesh deformation method boasting excellent robustness and quality-preserving characteristics [34–36]. Moreover, the method is completely generic, operating on point-clouds alone, and is perfectly parallel. The multiscale RBF method [33] is particularly effective, both increasing the computational efficiency and improving the system conditioning over conventional or reduced datapoint RBF methods, by using variable length scales depending on boundary point locations.

C. Search algorithm: SNOPT

The `SNOPT` [37] (Sparse Non-linear Optimiser) package is used here for gradient-based optimisation. This package implements a Sequential Quadratic Programming (SQP) algorithm for solving general non-linear constrained optimisation problems. The power of this package lies in its ability to efficiently and robustly handle large problems ($\approx$ 1000s of variables and constraints) while allowing precise constraint satisfaction.

The SQP algorithm operates iteratively whereby successive search directions are found from the solution of a quadratic programming (QP) sub-problem and a line-search is used to determine step length. In this work a non-derivative line-search is chosen. The sub-problems are formed from quadratic approximations to the augmented objective function (Lagrangian) and linearisations of the constraints. The quadratic approximation is initialised with an identity matrix and BFGS updates are used to approach the Hessian of the Lagrangian. The quadratic sub-problems are well-posed and the function values and derivatives thereof are easily evaluated; difficulty is not usually encountered when solving these sub-problems.

The use of the continuous adjoint for numerical gradients means that strict optimality convergence is not achievable and instead for this work optimisation is terminated by `SNOPT` when no further step can be taken. For all test cases here, the resulting solutions achieved at least an order of magnitude reduction in optimality and are feasible within a geometric tolerance of 1×10^{-6} and an aerodynamic tolerance of 1×10^{-4} (0.1 lift count).

D. Shape control

For compatible test cases, optimisation is performed using both the new generic modes and the traditional library-derived modes in order to assess the former in comparison with the latter. The mode shapes are used for deformative shape parameterisation where each design variable controls the amplitude of perturbation for an individual mode. In all cases, the mode shapes are used to parameterise both vertical and horizontal perturbation such that the number of design variables is twice the number of modes. All configurations are run across a range of control fidelities to assess the impact of the number of design variables, where the truncated basis is formed by taking the N modes corresponding to the lowest wave-numbers first.

Unless specified otherwise, the generic modes are run with the regularisation constraint which bounds the magnitude of design variables according to the singular value. Note that no equivalent constraint can be derived for the library-based modes since the corresponding singular values do not have a geometric meaning like in the case for the generic modes. Based on previous work with the gradient-limiting method [1] and the results of section V.C, the constraint parameter for the regularised generic modes is chosen to be $\mu = 150$ which gives a balance between geometric flexibility in representing all aerofoils while still constraining the design space by limiting contributions from small-wavelength modes.

VII. Aerodynamic Optimisation Results

In this section, three aerodynamic drag minimisation test cases are presented using the new generic modes for shape control. The focus of this work is the further development of the SVD modal approach to shape control, which is compared directly to the existing library-based state-of-the-art. For a comprehensive comparison of SVD modes to other shape control methods, the reader is directed to the work of Masters *et al.* [5, 11]. First, a standard aerofoil

drag minimisation in viscous transonic flow is considered, where the new generic modes are compared with the library-based modes and shown to be as effective despite requiring no geometry database. Second, the generic modes are demonstrated on a well-known academic test case highly reputed for its challenging geometry and flow behaviour. Again, the generic modes are compared with library-based modes and the effect of the design variable constraints is clearly demonstrated. Finally, a multi-body test case is presented with a geometry that does not conform to the standard aerofoil topology–where topology is used here in the general sense to include discrete surface features such as sharp points–and hence the library-based methodology is not applicable. Importantly, this demonstrates the flexibility of the new modal parameterisation by not requiring a geometry database and therefore being able to represent any geometry.

A. Test case 1: viscous aerofoil drag reduction

This standard aerofoil test case is one of several benchmark cases laid out by the AIAA Aerodynamic Design Optimisation Discussion Group (ADODG[†]) to aid in the collaborative evaluation and comparison among shape-optimisation practitioners. The case is defined as the drag minimisation of the RAE 2822 aerofoil in Mach 0.734 flow at a Reynolds number of 6.5×10^6 subject to constraints on volume (V), lift (C_L) and moment (C_M):

$$\begin{aligned} \min_{\alpha} \quad & C_D \\ \text{s.t.} \quad & C_L \geq 0.824 \\ & V \geq V_{initial} \\ & C_M \geq -0.092 \end{aligned} \tag{26}$$

Multiblock C-Grids extending to 100 chords are generated by transfinite interpolation with improved orthogonality and smoothness [38]. Three grid densities are considered here, summarised in Table 1, and shown in Figure 12 for the lowest density. Table 2 also shows the computed loads on the three meshes.

The finest grid is used for optimisation which is performed using both the new generic modes and the library-based modes. The generic modes are produced for a standard aerofoil topology with a single sharp point at the trailing edge and an interpolating condition at the leading edge and trailing edges as described in section V.A. See Figures 8 and 9 for the resulting mode shapes.

Table 2 summarises the optimised results obtained by each method across a sweep in number of modal design variables. Optimisation histories are shown in Figure 13 and the final optimised shapes and pressure distributions are shown in Figure 14. For this simple aerofoil case, it is clear that only a small number of design variables is required to parameterise the change in shape required. With only four modes, the upper surface shock is significantly weakened, and higher design fidelities are able to completely remove the shock within a small number of optimisation steps. With

[†]https://sites.google.com/view/mcgill-computational-aerogroup/adodg [retrieved July 2021]

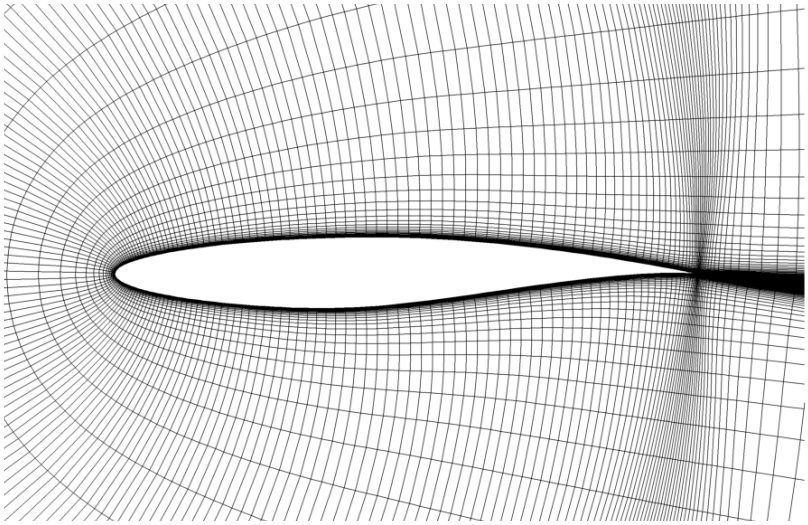

Fig. 12 (257 + 130) x 97 C-Grid around RAE2822 aerofoil, near-field view.

Table 1 RAE 2822 at $M = 0.734$, $Re = 6.5 \times 10^6$

Grid size $(n_{surf} + 2 \times n_{wake}) \times n_j$	C_L	C_D
$(257 + 130) \times 97$	0.8240	0.0214
$(385 + 194) \times 145$	0.8240	0.0206
$(513 + 258) \times 193$	0.8240	0.0199

16 modes, the optimised pressure distribution is noticeably smooth with a monotonic compression after the suction peak. This demonstrates the ability of the regularisation constraints to bound contributions from high-frequency shape modes while still making use of those modes for precise shape modifications.

With four modes (eight design variables), the library-based modes perform better than the new generic modes; this is expected since, as shown previously, the library-based modes have optimal compactness for the aerofoil database and hence can represent aerofoils with a very small number of design variables. However, at eight modes (sixteen design variables) and higher, the generic modes match the optimised result from the library-based modes. Interestingly the optimised solutions produced with the constrained generic modes achieve better feasibility tolerances than those produced with the unconstrained library-based modes; a possible explanation for this is that the constrained design space is smaller and hence the SQP method is better able to determine and satisfy the active set of constraints. Both the library-based modes and generic modes see little improvement in the optimised result beyond 12 modes, which reflects the simplicity of the shape change required for this test case. Importantly, for this representative aerofoil case, the generic modes have a similar design space compactness compared to the library-based modes but without requiring a geometry database. Hence, while not the focus of the current work, a comparison of the new SVD method with other shape control methods is expected to perform as well as the original library based approach, see [5, 11]. In the

following subsections, two non-trivial test cases are investigated where a database of representative geometry would not be suitable or available.

Table 2 Case 1 optimisation results

Number of modes	Drag (counts)		Non-linear feasibility	
	Library modes	Generic modes	Library modes	Generic modes
4	115.3	127.0	1.9×10^{-6}	7.1×10^{-6}
8	115.2	114.7	1.7×10^{-5}	3.5×10^{-8}
12	114.2	114.2	8.9×10^{-5}	2.9×10^{-8}
16	114.1	113.7	3.8×10^{-5}	6.9×10^{-7}

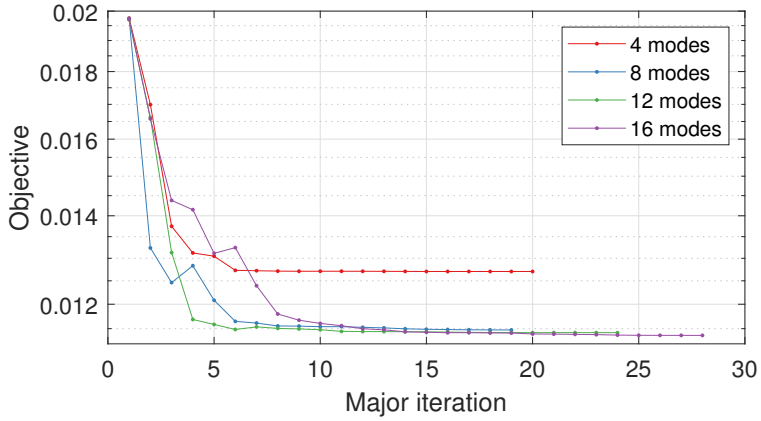

(a) Objective, drag coefficient

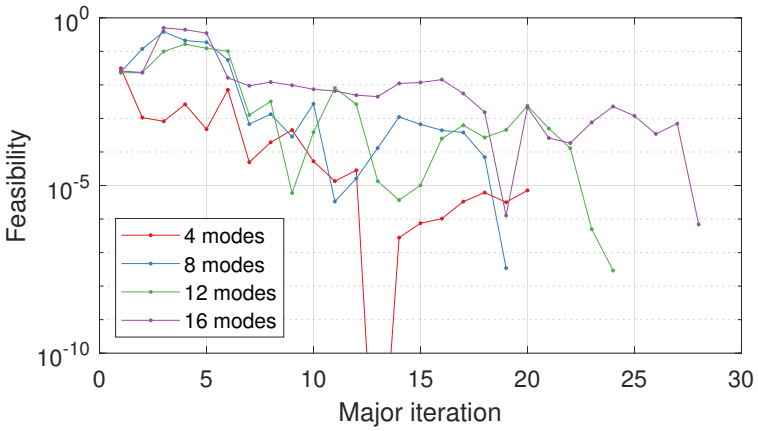

(b) Non-linear feasibility

Fig. 13 Optimisation convergence for test case 1 using generic modes

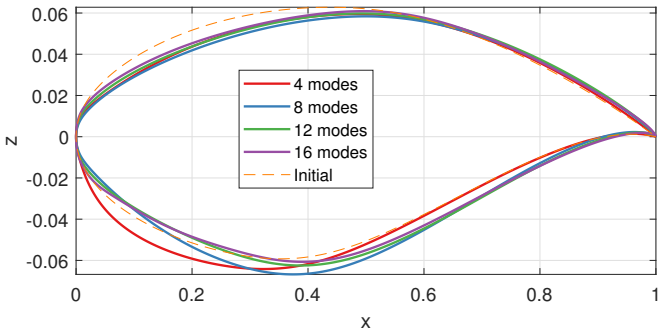

(a) Optimised shapes

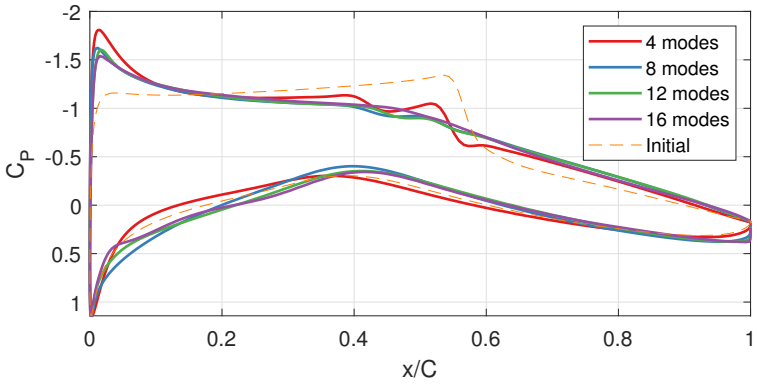

(b) Optimised pressure distributions

Fig. 14 Optimised results for test case 2 using generic modes

B. Test case 2: inviscid transonic drag reduction

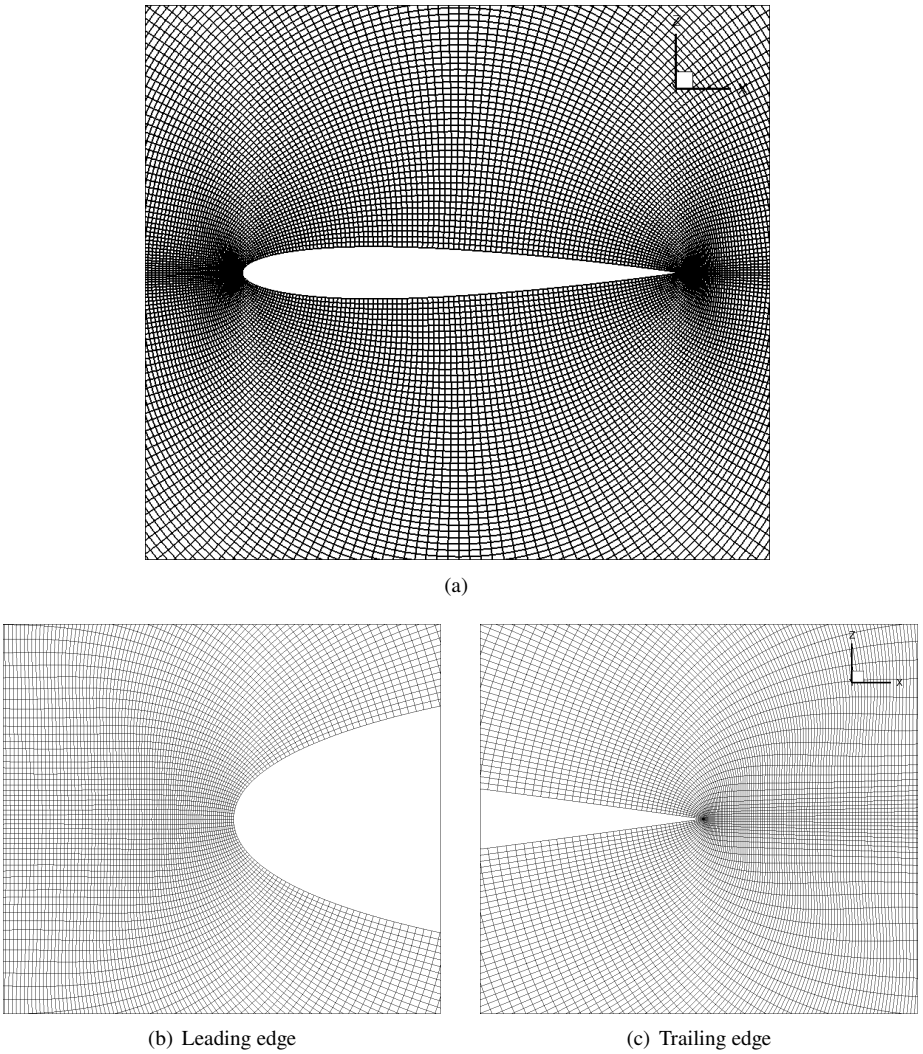

(a)

(b) Leading edge

(c) Trailing edge

Fig. 15 513×257 **O-Mesh generated around NACA 0012 aerofoil**

This case, also from the ADODG set of benchmarks, is defined as minimising the inviscid drag at Mach 0.85 and 0 degree incidence subject to the constraint that the solution shape must lie outside the profile of the initial shape, a NACA0012 aerofoil:

$$\begin{aligned} \min_{\alpha} \quad & C_D \\ \text{s.t.} \quad & z \geq z_0 \end{aligned} \tag{27}$$

This case is chosen since it has been studied extensively in the literature due to the unique aerodynamic and geometric challenges it poses. In fact, from a geometric standpoint it is one of the most challenging test cases possible and so makes an ideal benchmark to demonstrate the current method. Despite being an inviscid problem this does not restrict applicability to RANS-based objectives, as shown for test case 1, which generally present as better-conditioned

optimisation problems than Euler-based ones due to the additional physical modelling and removal of non-unique solutions. This problem was formulated by Vassberg [39] specifically for studying different optimisation methods since it permits a large design space and requires only moderate computational expense. The case only exhibits drag due to shocks, with Vassberg stating that a shock-free design is anticipated to be impossible. Starting from a baseline of 469 drag counts, Vassberg achieved an optimised result of 103.8 drag counts while also identifying a pathological nature in the symmetric problem in the form of asymmetric instability. A detailed study by Destarac *et al.* [40] additionally demonstrated Mach hysteresis in various optimised shapes due to the existence of non-unique flow solutions. In addition to these numerical challenges, the associated geometric problem is demanding, requiring a high-fidelity and flexible design space as well as a robust and quality-preserving mesh deformation method.

Poole *et al.* [41] used orthogonal modes extracted by singular value decomposition, achieving 85.6 drag counts with only 15 design variables. Carrier *et al.* [26] apply several different optimisation frameworks, eventually obtaining a result of 36.7 drag counts, 1.1 drag counts of which they show corresponds to spurious drag. He *et al.* [42] use a volume B-Spline obtaining a result of 7.60 drag counts with 50 design variables, the lowest published result for comparable mesh resolution (131K cells).

Masters *et al.* compared six different parameterisations on the benchmark problem [5] as well as applying a multilevel subdivision parameterisation [43]. The authors achieved a result of 27.8 drag counts on a 257×257 mesh using single-level B-Splines (16 design variables) and a result of 15.7 drag counts on the same mesh using multilevel subdivision curves; when performed on a 1025×513 mesh the multilevel subdivision scheme was able achieve 4.2 drag counts. Two distinct solution shapes were observed by the authors differing in boat-tail angle and thickness, where the thicker shapes with larger-boat tail angles corresponded to different trailing-edge flow structures with lower overall inviscid drag. Previous work by the authors using the gradient-limiting methodology achieved a value of 7.88 drag counts on a 513×257 grid and a value of 1.60 drag counts on a 1025×513 grid [1]. Two techniques found to be particularly effective by Masters *et al.* [43] for this test case are also used here: first, the explicit imposition of a symmetry boundary condition on the volume mesh to stabilise convergence of the flow; and second, the use of flow-restarts during optimisation to minimise the influence of flow hysteresis during line-searches.

Table 3 Case 2 optimisation results

Number of modes	**Drag (counts)**		
	Library modes	**Generic modes (unconstrained)**	**Generic modes (constrained)**
8	67.16	15.00	25.46
16	13.42	9.16	7.64
32	24.31	74.10	5.44
64	178.58	82.72	5.15

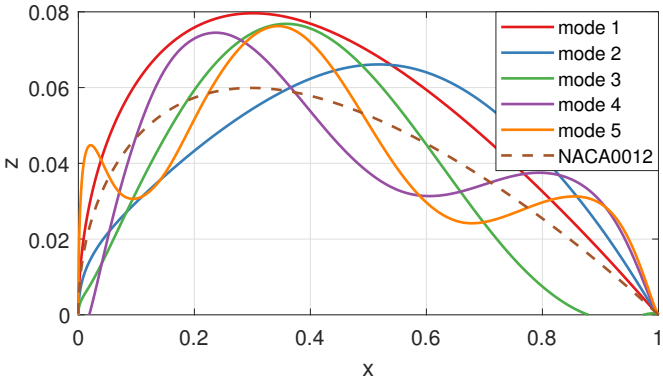

(a) Library-based modes

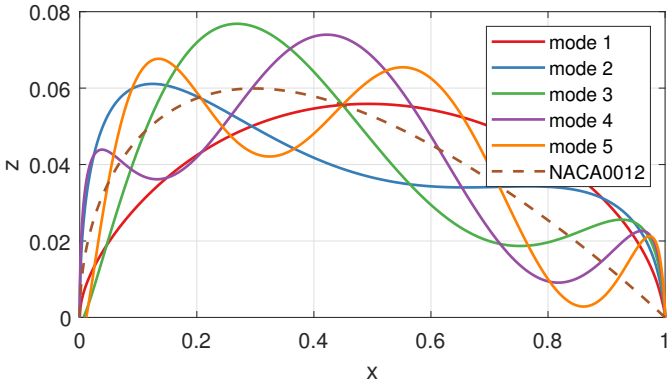

(b) Generic modes

Fig. 16 Optimisation convergence for test case 2

Figure 16 shows the mode shapes produced for both the new generic modes and the traditional library-based modes applied as thickness perturbations to the NACA 0012 aerofoil. Figure 17 shows the optimisation convergence and Table 3 summarises the optimised results for three different shape control approaches: library-based modes; the new generic modes without bound constrains and; the new generic modes with bounds constraints. It is immediately evident that the singular value regularisation constraints improve the optimisation both in terms of convergence rate as well as final result. As was shown for the original gradient-limiting approach, the additional geometric constraints result in the optimisation convergence rate being largely independent of the number of design variables and also better results at high control fidelity by avoiding spurious local minima. Hence the geometrically-derived generic modes with singular value constraints are able to regularise the optimisation problem by constraining the design space in the same way as the original gradient-limiting approach. In comparison, the traditional library-based modes perform similarly to the generic modes without regularisation constraints, suffering from deteriorated convergence rate at higher fidelities and premature termination at local minima with non-physical geometries.

Figures 18 shows the optimised shapes produced across all configurations. In the cases of the unconstrained generic modes and the traditional library-based modes the difficulties encountered as the control fidelity increases

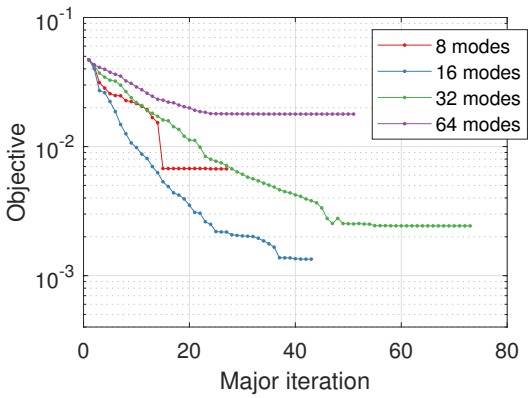

(a) Library-based modes

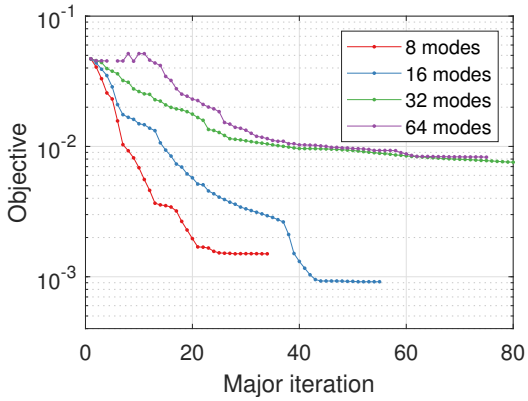

(b) Generic modes (unconstrained)

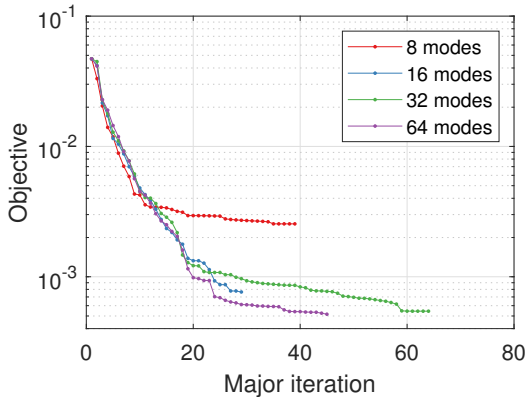

(c) Generic modes (constrained)

Fig. 17 Optimisation convergence for test case 2

become clear. In particular, non-smooth geometries are produced which here refers specifically to the presence of pathological short-wavelength features and surface oscillations. The latter are particularly evident when considering the corresponding pressure distributions, shown in Figure 19, due to the relationship between surface curvature and pressure distribution variation. Similarly, the unconstrained configurations are seen to result in a feature forming at the trailing edge in response the the initial shock location. This undesirable geometric feature invariably leads to a strong local minima and a suboptimal result. By contrast, the generic modes in combination with the singular value regularisation constraints lead to a well-defined solution with a visually smooth pressure distribution.

Figure 20 shows the regularisation constraint bound and design variable values for the constrained generic modes at the highest fidelity case $N_{mode} = 64$ where the effect of the regularising constraint bound is made clear in constraining the magnitude of modal design variables in an inverse relation to the wave number of the mode.

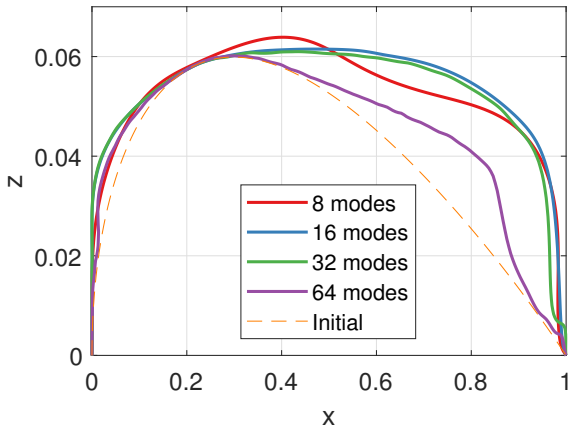

(a) Library-based modes

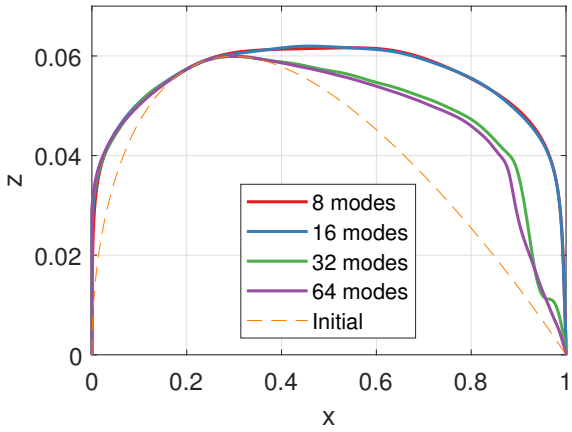

(b) Generic modes (Unconstrained)

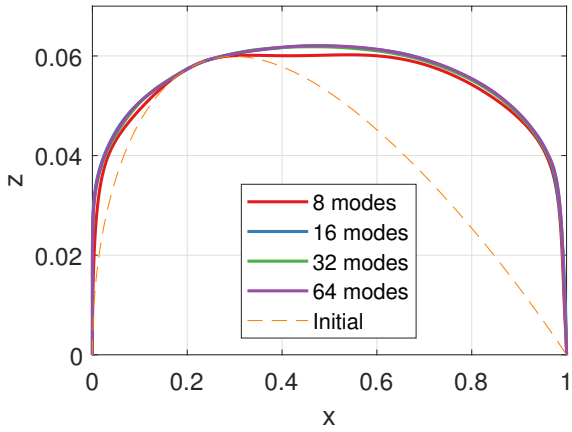

(c) Generic modes (Constrained)

Fig. 18 Optimised shapes for test case 2

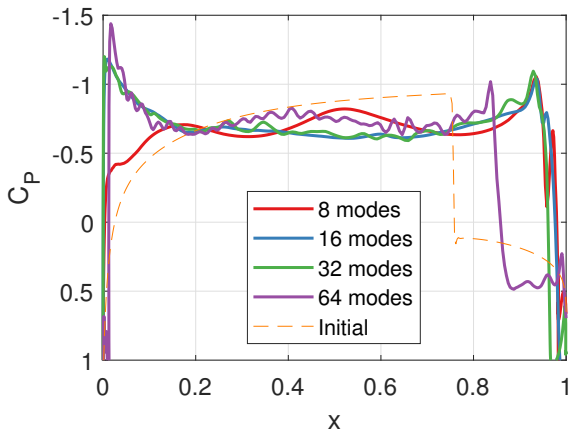

(a) Library-based modes

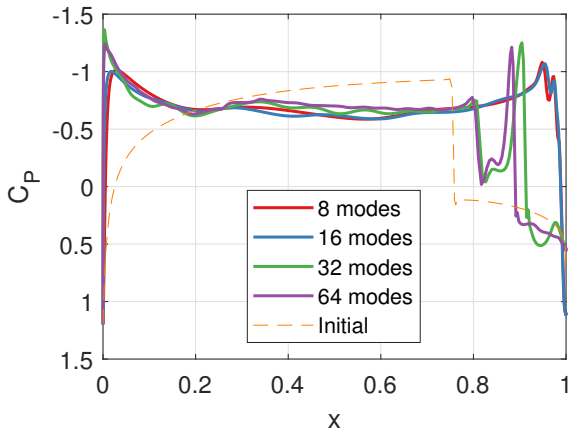

(b) Generic modes (Unconstrained)

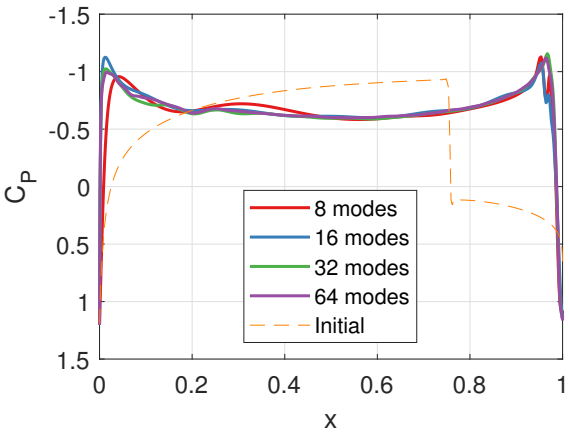

(c) Generic modes (Constrained)

Fig. 19 Optimised pressure distributions for test case 2

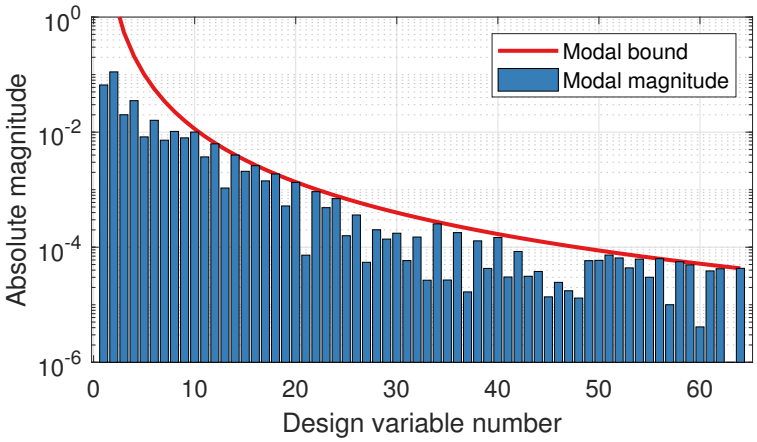

(a) Chordwise (x)

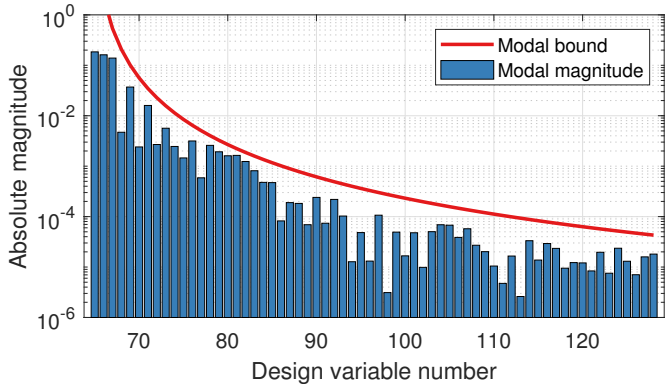

(b) Vertical (z)

Fig. 20 Optimised design variables for test case 2, $N_{mode} = 64$

C. Test case 3: inviscid biplane drag reduction

This test case, the drag minimisation of a fixed-area biplane profile at Mach 2.0, originally derives from a result presented by Busemann at the 5th Volta conference on high speed flows [44] showing that wave drag can be cancelled using a biplane configuration. More recently, this test problem has been applied uniquely to the investigation of aerodynamic topology optimisation [28, 45] where the number of aerodynamic bodies and the presence of discrete features are represented in a unified parameterisation. Formally, the case is defined as minimising the inviscid drag at Mach 2.00 and 0 degree incidence subject to the constraint on total internal volume:

$$\begin{aligned} \min_{\alpha} \quad & C_D \\ \text{s.t.} \quad & V \geq V_0 \end{aligned} \tag{28}$$

In this work, the two-body symmetric biplane configuration is investigated where the shape of a single plane is parameterised for drag minimisation. The resulting single plane geometry is meshed using a block structured mesh with a symmetry plane at $z = 0$ to simulate the symmetric biplane configuration. The initial baseline geometry is chosen to be a parabolic profile with internal volume matching that of the constraint and a separation of 0.6 chords between the two planes.

This test case is chosen since it represents an unconventional geometric configuration for which there is no historic database that can be used to generate traditional SVD modes. Unlike typical aerofoils, each plane in the configuration has two discrete features, a sharp point at the leading and trailing edges, and hence can't be parameterised easily with modes derived from an aerofoil database. This highlights the flexibility and generality afforded by the new generic modes which can be derived for any shape or topological configuration. Following the formulation given in section IV.D, discrete sharp points are easily incorporated into the generic modal basis at the leading and trailing edges. Unlike the previous test cases, this test case does not have any fixed-points and hence piecewise linear modes are produced in the modal basis that allow shearing and uniform translation of all surface points.

For low values of the internal volume constraint V_0, there is an optimum non-lifting profile known as the Busemann Biplane which exploits shock cancellations that can occur between the two planes. This biplane formulation lends itself well to numerical optimisation, particularly for higher values of V_0 where a trade-off is required between exploiting shock cancellations and avoiding choking of the flow and the consequent generation of a large bow shock. Consequently, a higher value of $V_0 = 0.12$ is chosen here for which the Busemann profile is not optimal due to choking of the flow.

As previously, the optimisation is performed across a sweep in the number of design variables to assess the effect of design fidelity on the optimisation process and final result. Figure 21 shows the optimisation objective convergence history for each design fidelity tested and figure 22 shows the resulting optimised shapes. Table 4 summarises the final optimised objectives and non-linear feasibilities for each case. For all cases the volume constraint is satisfied within

the geometric tolerance (1×10^{-6}). For this test case, the final result is dependent on the chosen design fidelity where increasing the number of design variables leads to a monotonic improvement in the optimised objective. As with the previous test cases, the initial rate of optimisation convergence is independent of the number of design variables.

Table 4 Case 3 optimisation results

Number of modes	**Objective** (Drag counts)	**Feasibility**
8	234.34	1.00E-06
16	213.00	1.00E-06
32	192.30	4.35E-08
64	145.84	1.04E-07
96	130.86	1.10E-08

From the corresponding optimised shapes (Figure 22) it is clear that increasing the design fidelity provides better resolution for the inside geometry of the biplane. In particular, the higher fidelity provided by the shorter wavelength modes allows better resolution of the angular-type features used for shock cancellations between the two planes. Moreover, the optimisation has exploited the two piecewise linear modes that allow rigid-body motion to alter the vertical position of the biplane in order to better align the internal shocks and expansions. Importantly, and unlike other shape control methods, these translation-enabling modes arise naturally as part of the generic methodology such that they incorporate the specified boundary conditions while remaining orthogonal to the full basis. At the highest fidelity (96 modes) the optimised shape resembles the triangular Busemann biplane but with a curved external surface instead of a flat one which is required to avoid choking the flow between the two planes. Figure 23 shows the resulting flow fields for the initial geometry and the optimised one with 96 modes where cancellation of the leading-edge shock is shown clearly. The effect of shock cancellations can also be visualised by the entropy generation that occurs across the biplane configuration; this is shown in Figure 24 for each design fidelity level where the change in entropy is expressed non-dimensionally by:

$$\frac{P/\rho^{\gamma}}{P_{\infty}/\rho_{\infty}^{\gamma}} - 1 \tag{29}$$

Here the effect of increasing design fidelity is clear where there is progressively less of an increase in entropy for the optimised design compared to the baseline as the number of design variables increases.

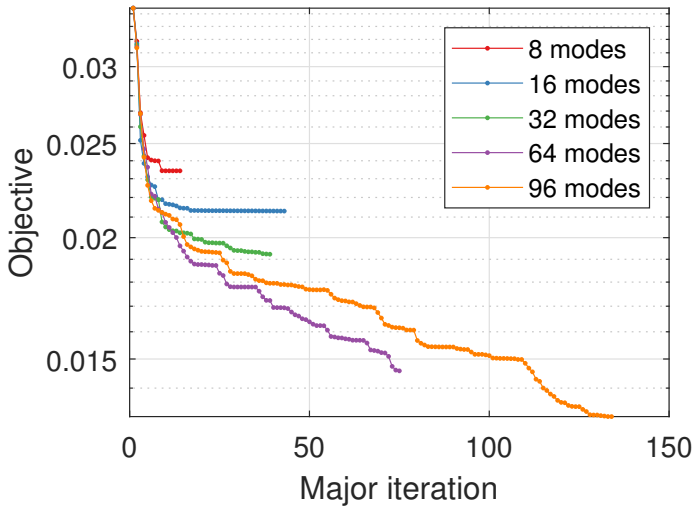

Fig. 21 Optimisation convergence for test case 3

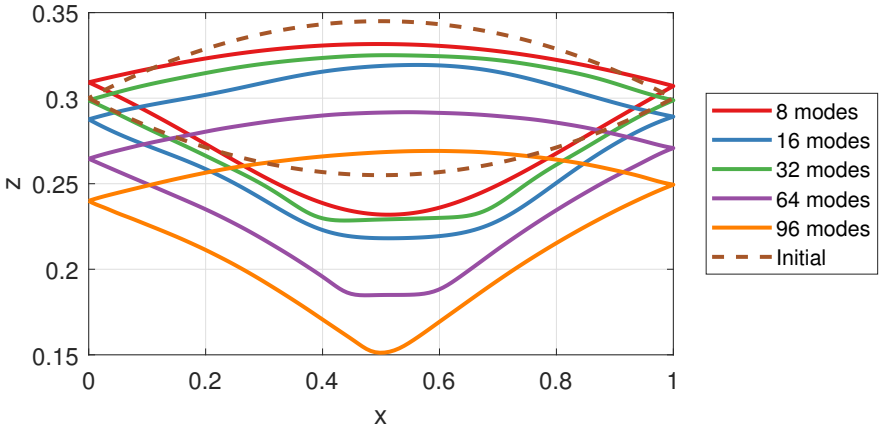

Fig. 22 Optimised shapes for test case 3

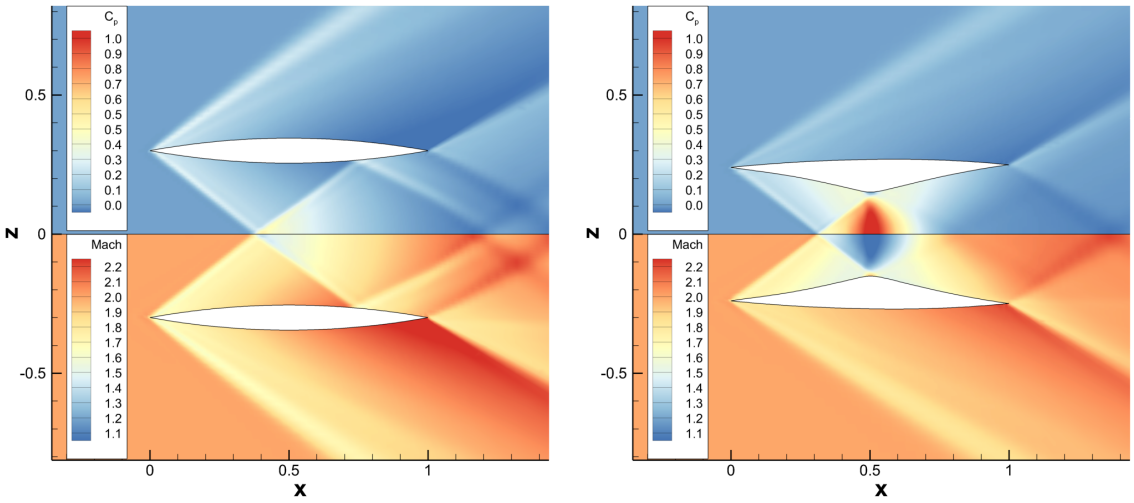

(a) Initial

(b) Optimised, $N_{mode} = 96$

Fig. 23 Flow field comparison for test case 3

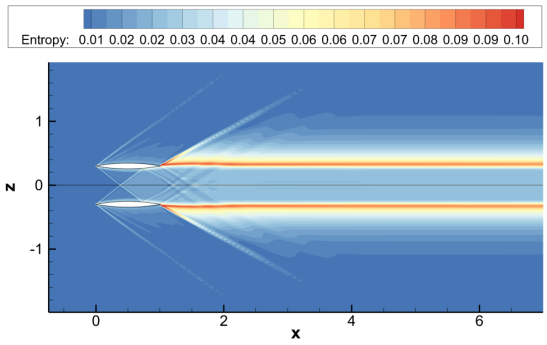

(a) Initial

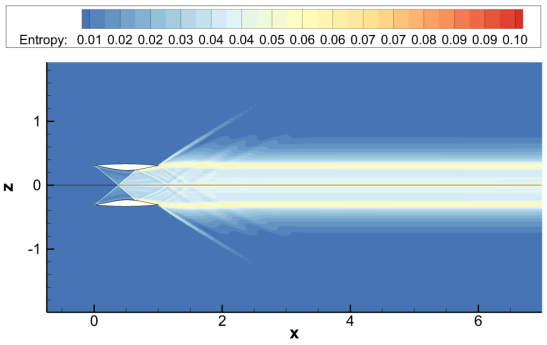

(b) Optimised, N_{mode} = 8

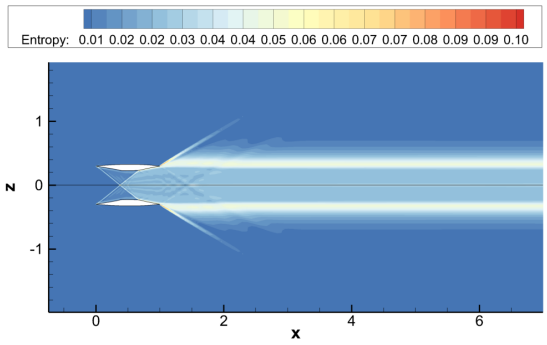

(c) Optimised, N_{mode} = 16

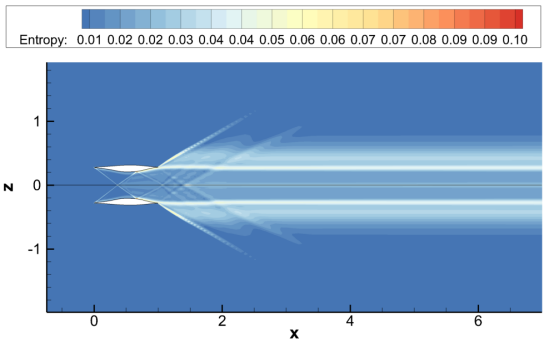

(d) Optimised, N_{mode} = 32

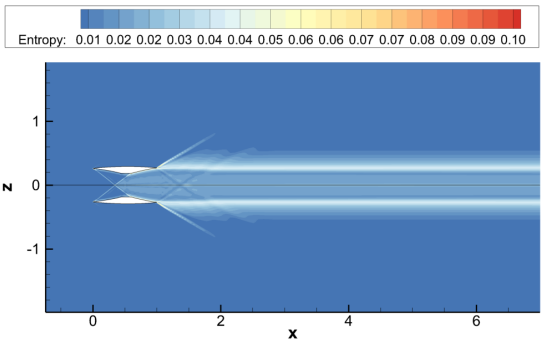

(e) Optimised, N_{mode} = 64

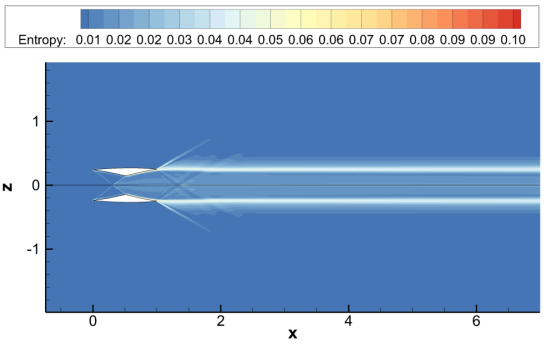

(f) Optimised, N_{mode} = 96

Fig. 24 Change in entropy for test case 3

VIII. Conclusions

A new methodology for generating orthogonal shape modes for aerodynamic optimisation has been presented which does not require training data and which generalises to arbitrary topologies. The new methodology is a further development of the gradient-limiting method of the authors which aims to regularise high-fidelity shape optimisation problems using a surface smoothness constraint. Importantly, since the modes are derived entirely from a surface differencing operator, no training database is required and there is no restriction on the topology for which modal design variables can be generated. Despite requiring no training data, the generic modes can form a compact basis for geometric data as demonstrated here on an aerofoil library. The geometry based derivation naturally leads to translational modes as part of the orthogonal basis and can be easily extended to produce mode shapes for surfaces in three-dimensions using a differencing operator for the surface representation.

Moreover, derivation of the mode shapes from a geometric differencing operator leads to a natural design variable bound for constraining surface smoothness during optimisation. As with the original gradient-limiting approach, this has the effect of regularising the shape optimisation problem by constraining the design space in a geometrically meaningful manner.

Applying the new shape control methodology on standard aerodynamic optimisation test cases demonstrates the regularising design variable bounds to have an equivalent effect to that of the previous gradient limiting approach; the optimisation convergence rate is independent of the number of design variables and the optimised objective at high design fidelities is greatly improved by avoiding local minima corresponding to spurious geometries. As a result, the new generic shape modes used with regularising design variable constraints achieves 5.15 drag counts for the AIAA ADODG test case 1, which is the lowest result published for equivalent mesh resolution. The generic modes have also been applied to a non-standard aerodynamic test case, highlighting the geometric flexibility of the new method for non-standard configurations and the efficacy of high-fidelity shape parameterisations for aerodynamic optimisation.

Acknowledgments

This work was carried out using the computational facilities of the Advanced Computing Research Centre, University of Bristol - http://www.bristol.ac.uk/acrc. This work was funded through an EPSRC Doctoral Training Grant.

References

[1] Kedward, L. J., Allen, C. B., and Rendall, T. C. S., "Gradient-Limiting Shape Control for Efficient Aerodynamic Optimization," *AIAA Journal*, Vol. 58, No. 9, 2020, pp. 3748–3764. URL https://doi.org/10.2514/1.J058977.

[2] Wu, N., Mader, C., and Martins, J. R., "Sensitivity-based Geometric Parameterization for Aerodynamic Shape Optimization," *AIAA AVIATION Forum*, Chicago, IL, 2022. URL https://doi.org/10.2514/6.2022-3931.

[3] Reuther, J., and Jameson, A., "A Comparison of Design Variables for Control Theory Based Airfoil Optimization," *Technical Report, NASA Research Institute for Advanced Computer Science*, 1995.

[4] Castonguay, P., and Nadarajah, S., "Effect of Shape Parameterization on Aerodynamic Shape Optimization," *45th AIAA Aerospace Sciences Meeting and Exhibit*, 2007, pp. 1–20. URL https://doi.org/10.2514/6.2007-59.

[5] Masters, D. A., Poole, D. J., Taylor, N. J., Rendall, T. C. S., and Allen, C. B., "Influence of Shape Parameterization on a Benchmark Aerodynamic Optimization Problem," *Journal of Aircraft*, Vol. 54, No. 6, 2017, pp. 2242–2256. URL https://doi.org/10.2514/1.C034006.

[6] Drela, M., "Pros & Cons of Airfoil Optimization," *Frontiers of Computational Fluid Dynamics*, edited by D. A. Caughey and M. M. Hafez, World Scientific, 1998. URL https://doi.org/10.1142/9789812815774_0019.

[7] Kedward, L., Allen, C. B., and Rendall, T., "Gradient-Limiting Shape Control for Efficient Aerodynamic Optimisation," *2018 Applied Aerodynamics Conference*, 2018, pp. 1–22. URL https://doi.org/10.2514/6.2018-3951.

[8] Kedward, L., Allen, C., and Rendall, T., "Gradient-Limiting Shape Optimisation Applied to AIAA ADODG Test Cases," *AIAA Scitech 2019 Forum*, American Institute of Aeronautics and Astronautics Inc. (AIAA), 2019. URL https://doi.org/10.2514/6.2019-1209.

[9] Poole, D. J., Allen, C. B., and Rendall, T. C. S., "Metric-Based Mathematical Derivation of Efficient Airfoil Design Variables," *AIAA Journal*, Vol. 53, No. 5, 2015, pp. 1349–1361. URL https://doi.org/10.2514/1.J053427.

[10] Poole, D. J., Allen, C. B., and Rendall, T. C., "High-fidelity aerodynamic shape optimization using efficient orthogonal modal design variables with a constrained global optimizer," *Computers and Fluids*, Vol. 143, 2017, pp. 1–15. URL https://doi.org/10.1016/j.compfluid.2016.11.002.

[11] Masters, D. A., Taylor, N. J., Rendall, T., Allen, C. B., and Poole, D. J., "A Geometric Comparison of Aerofoil Shape Parameterisation Methods," *AIAA Journal*, Vol. 55, No. 5, 2017, pp. 1575–1589. URL https://doi.org/10.2514/1.J054943.

[12] Braibant, V., and Fleury, C., "Shape optimal design using B-splines," *Computer Methods in Applied Mechanics and Engineering*, Vol. 44, No. 3, 1984, pp. 247–267. URL https://doi.org/10.1016/0045-7825(84)90132-4.

[13] Sederberg, T. W., and Parry, S. R., "Free-form deformation of solid geometric models," *ACM SIGGRAPH Computer Graphics*, Vol. 20, No. 4, 1986, pp. 151–160. URL https://doi.org/10.1145/15886.15903.

[14] Hicken, J. E., and Zingg, D. W., "Aerodynamic Optimization Algorithm with Integrated Geometry Parameterization and Mesh Movement," *AIAA Journal*, Vol. 48, No. 2, 2010, pp. 400–413. URL https://doi.org/10.2514/1.44033.

[15] Morris, A. M., Allen, C. B., and Rendall, T. C. S., "Domain-Element Method for Aerodynamic Shape Optimization Applied to a Modern Transport Wing," *AIAA Journal*, Vol. 47, No. 7, 2009, pp. 1647–1659. URL https://doi.org/10.2514/1.39382.

[16] Hicks, R. M., and Henne, P. A., "Wing Design by Numerical Optimization," *Journal of Aircraft*, Vol. 15, No. 7, 1978, pp. 407–412. URL https://doi.org/10.2514/3.58379.

[17] Kulfan, B. M., "A Universal Parametric Geometry Representation Method – " CST "," *45th AIAA Aerospace Sciences Meeting and Exhibit*, 2007. URL https://doi.org/10.2514/1.29958.

[18] Belegundu, A., and Rajan, S. D., "A shape optimization approach based on natural design variables and shape functions," *Computer Methods in Applied Mechanics and Engineering*, Vol. 66, No. 1, 1988, pp. 87–106. URL https://doi.org/10.1016/0045-7825(88)90061-8.

[19] Robinson, G. M., and Keane, A. J., "Concise Orthogonal Representation of Supercritical Airfoils," *Journal of Aircraft*, Vol. 38, No. 3, 2008, pp. 580–583. URL https://doi.org/10.2514/2.2803.

[20] Toal, D., Bressloff, N., and Keane, A., "Geometric Filtration Using POD for Aerodynamic Design Optimization," 2012, pp. 1–13. URL https://doi.org/10.2514/6.2008-6584.

[21] Poole, D. J., Allen, C. B., and Rendall, T., "Control Point-Based Aerodynamic Shape Optimization Applied to AIAA ADODG Test Cases," *53rd AIAA Aerospace Sciences Meeting*, , No. January, 2015, pp. 1–20. URL https://doi.org/10.2514/6.2015-1947.

[22] Allen, C. B., Poole, D. J., and Rendall, T. C. S., "Wing aerodynamic optimization using efficient mathematically-extracted modal design variables," *Optimization and Engineering*, Vol. 19, 2018, pp. 453–477. URL https://doi.org/10.1007/s11081-018-9376-7.

[23] Poole, D., Allen, C., and Rendall, T., *AIAA Scitech 2019 Forum*, American Institute of Aeronautics and Astronautics Inc. (AIAA), United States, 2019. doi:10.2514/6.2019-1701, URL https://scitech.aiaa.org/, aIAA Scitech Forum, 2019 ; Conference date: 07-01-2019 Through 11-01-2019.

[24] Cinquegrana, D., and Iuliano, E., "Efficient Global Optimization of a Transonic Wing with Geometric Data Reduction," , No. February 2019, 2017. URL https://doi.org/10.2514/6.2017-3057.

[25] Ghoman, S., Sarhaddi, D., Chen, P., Wang, Z., and Kapania, R., "A Hybrid Optimization Strategy Using Design-Space Evolution and POD-based Order Reduction," , No. September, 2012, pp. 1–16. URL https://doi.org/10.2514/6.2012-5631.

[26] Carrier, G., Destarac, D., Dumont, A., Meheut, M., Salah El Din, I., Peter, J., Ben Khelil, S., Brezillon, J., and Pestana, M., "Gradient-Based Aerodynamic Optimization with the elsA Software," *52nd AIAA Aerospace Sciences Meeting*, 2014, pp. 1–31. URL https://doi.org/10.2514/6.2014-0568.

[27] Eckart, C., and Young, G., "The approximation of one matrix by another of lower rank," *Psychometrikaa*, Vol. 1, 1936, pp. 211–218. URL https://doi.org/10.1007/BF02288367.

[28] Kedward, L., Payot, A. D., Rendall, T., and Allen, C. B., "Efficient Multi-Resolution Approaches for Exploration of External Aerodynamic Shape and Topology," *2018 Applied Aerodynamics Conference*, Atlanta, Georgia, 2018. URL https://doi.org/10.2514/6.2018-3952.

[29] Kulfan, B., and Bussoletti, J., ""Fundamental" Parameteric Geometry Representations for Aircraft Component Shapes," *11th AIAA/ISSMO Multidisciplinary Analysis and Optimization Conference*, 2006. URL https://doi.org/10.2514/6.2006-6948.

[30] Palacios, F., Colonno, M. R., Aranake, A. C., Campos, A., Copeland, S. R., Economon, T. D., Lonkar, A. K., Lukaczyk, T. W., Taylor, T. W. R., and Alonso, J. J., "Stanford University Unstructured (SU2): An open-source integrated computational environment for multi-physics simulation and design," *51st AIAA Aerospace Sciences Meeting*, 2013. URL https://doi.org/10.2514/6.2013-287.

[31] Economon, T. D., Alonso, J. J., Albring, T. A., and Gauger, N. R., "Adjoint Formulation Investigations of Benchmark Aerodynamic Design Cases in SU2," *35th AIAA Applied Aerodynamics Conference*, 2017, pp. 1–13. URL https://doi.org/10.2514/6.2017-4363.

[32] Spalart, P., and Allmaras, S., "A one-equation turbulence model for aerodynamic flows," *30th Aerospace Sciences Meeting and Exhibit*, 1992. URL https://doi.org/10.2514/6.1992-439.

[33] Kedward, L., Allen, C. B., and Rendall, T. C., "Efficient and exact mesh deformation using multiscale RBF interpolation," *Journal of Computational Physics*, Vol. 345, 2017, pp. 732–751. URL https://doi.org/10.1016/j.jcp.2017.05.042.

[34] de Boer, A., van der Schoot, M. S., and Bijl, H., "Mesh deformation based on radial basis function interpolation," *Computers and Structures*, Vol. 85, No. 11-14, 2007, pp. 784–795. URL https://doi.org/10.1016/j.compstruc.2007.01.013.

[35] Rendall, T. C. S., and Allen, C. B., "Unified fluid-structure interpolation and mesh motion using radial basis functions," *International Journal for Numerical Methods in Engineering*, Vol. 74, No. 10, 2008. URL https://doi.org/10.1002/nme.2219.

[36] Rendall, T. C., and Allen, C. B., "Reduced surface point selection options for efficient mesh deformation using radial basis functions," *Journal of Computational Physics*, Vol. 229, No. 8, 2010, pp. 2810–2820. URL https://doi.org/10.1016/j.jcp.2009.12.006.

[37] Gill, P. E., Murray, W., and Saunders, M. A., "SNOPT: An SQP Algorithm for Large-Scale Constrained Optimization," *SIAM Review*, Vol. 47, No. 1, 2005, pp. 99–131. URL https://doi.org/10.1137/S0036144504446096.

[38] Allen, C. B., "Towards automatic structured multiblock mesh generation using improved transfinite interpolation," *International Journal for Numerical Methods in Engineering*, Vol. 74, No. 5, 2007, pp. 697–733. URL https://doi.org/10.1002/nme.2170.

[39] Vassberg, J., Harrison, N., Roman, D., and Jameson, A., "A Systematic Study on the Impact of Dimensionality for a Two-Dimensional Aerodynamic Optimization Model Problem," *29th AIAA Applied Aerodynamics Conference*, 2011, pp. 1–19. URL https://doi.org/10.2514/6.2011-3176.

[40] Destarac, D., Carrier, G., Anderson, G. R., Nadarajah, S., Poole, D. J., Vassberg, J. C., and Zingg, D. W., "Example of a Pitfall in Aerodynamic Shape Optimization," *AIAA Journal*, Vol. 56, No. 4, 2018, pp. 1–9. URL https://doi.org/10.2514/1.J056128.

[41] Poole, D. J., Allen, C. B., and Rendall, T., "Control Point-Based Aerodynamic Shape Optimization Applied to AIAA ADODG Test Cases," *53rd AIAA Aerospace Sciences Meeting*, 2015. URL https://doi.org/10.2514/6.2015-1947.

[42] He, X., Li, J., Mader, C. A., Yildirim, A., and Martins, J. R., "Robust aerodynamic shape optimization—From a circle to an airfoil," *Aerospace Science and Technology*, Vol. 87, 2019, pp. 48 – 61. URL https://doi.org/10.1016/j.ast.2019.01.051.

[43] Masters, D. A., Taylor, N. J., Rendall, T. C. S., and Allen, C. B., "Multilevel Subdivision Parameterization Scheme for Aerodynamic Shape Optimization," *AIAA Journal*, Vol. 55, No. 10, 2017, pp. 1–16. URL https://doi.org/10.2514/1.J055785.

[44] Ferrari, C., "Recalling the Vth Volta Congress: High Speeds in Aviation," *Annual Review of Fluid Mechanics*, Vol. 28, No. 1, 1996, pp. 1–9. doi:10.1146/annurev.fl.28.010196.000245, URL https://doi.org/10.1146/annurev.fl.28.010196.000245.

[45] Payot, A. D., Rendall, T. C., and Allen, C. B., "Restricted snakes volume of solid (RSVS): A parameterisation method for topology optimisation of external aerodynamics," *Computers and Fluids*, Vol. 182, 2019, pp. 60–84. URL https://doi.org/10.1016/j.compfluid.2019.02.008.